Chemical Geology 554 (2020) 119799

Contents lists available at ScienceDirect

Chemical Geology

journal homepage: www.elsevier.com/locate/chemgeo

Intra-tooth stable isotope profiles in warthog canines and third molars: Implications for paleoenvironmental reconstructions

Deming Yang[a,*], Kevin T. Uno[b], Antoine Souron[c], Kate McGrath[c,d], Éric Pubert[c], Thure E. Cerling[e]

[a] Interdepartmental Doctoral Program in Anthropological Sciences, Stony Brook University, Stony Brook, NY 11794, United States
[b] Division of Biology and Paleo Environment, Lamont-Doherty Earth Observatory of Columbia University, Palisades, NY 10964, United States
[c] UMR CNRS 5199, PACEA, Université de Bordeaux, 33615 Pessac, France
[d] Center for the Advanced Study of Human Paleobiology, Department of Anthropology, The George Washington University, Washington, DC 20052, United States
[e] Department of Geology and Geophysics, University of Utah, Salt Lake City, UT 84112, United States

ARTICLE INFO

Editor: Michael E. Böttcher

Keywords:
Phacochoerus africanus
Stable isotope ecology
Enamel histology
Dietary interpretation
Seasonality

ABSTRACT

Intra-tooth stable isotope variations have been used to interpret seasonality and aridity in paleoenvironmental reconstructions of paleontological and archeological sites. However, most intra-tooth datasets only permit qualitative interpretations of seasonality, because the measured signal is attenuated due to the duration of enamel mineralization process and sampling geometry. The common warthog (*Phacochoerus africanus*) is an ideal organism to investigate stable isotope variation in enamel. Their canines grow continuously through the life of the individual and are therefore excellent candidates for mathematical modeling of seasonal signals and of signal attenuation; further, their isotope profiles (a series of isotope measurements) can be compared to isotope profiles of third molars (M3) to provide insights into environmental reconstructions. We first obtained paired intra-tooth enamel samples from ever-growing canines and hypsodont M3s of two extant common warthog specimens from Laikipia, Kenya. Second, from a different set of specimens, we collected data on enamel growth patterns and geometry using histological thin sections and transmitted light microscopy, and enamel mineralization parameters using micro-CT scans in each tooth type. Third, we reconstructed the timeline of unattenuated seasonal $\delta^{18}O$ signal from canine enamel using growth rate estimates and the inverse model of Passey et al. (2005). Our results demonstrate that canines, which capture ~1.5 years of time, exhibit near-constant growth rates and simple enamel maturation geometry, whereas M3s, which also represent ~1.5 years of time, exhibit linearly decreasing growth rates and more complex maturation patterns. We compare the timelines of unattenuated seasonal $\delta^{18}O$ signal and measured M3 profiles and find an average signal reduction of ~50% in the M3s, providing interpretations of the duration of seasonal cycles that are consistent 75% of the time. We conclude that warthog canines are well suited for the inverse model approach, and we established the model parameters for the forward and inverse methods. Timeline reconstructions based on M3 histology are promising for investigating the pattern of rainfall seasonality in the past. Finally, we found an unexpected carbon isotopic spacing of ~2‰ between canine and M3 enamel, which suggests caution in interpreting $\delta^{13}C$ results from suid canine or molar enamel alone.

1. Introduction

Among extant suids (family Suidae), the common warthog (*Phacochoerus africanus*) and the desert warthog (*Phacochoerus aethiopicus*) are frequently found in the African savanna ecosystems (d'Huart and Grubb, 2001; Kingdon, 1988). Warthogs are highly specialized herbivores (unlike most other extant suids that are omnivorous); their diet specialization is reflected by their elongated and hypsodont third molars (M3s) that are adapted to abrasive diets such as grasses (Cooke and Wilkinson, 1978; Field, 1972; Rodgers, 1984; Souron, 2017). Warthogs are important reference species in paleoecological studies both for interpreting fossil suid ecology (Bishop et al., 2006; Harris and Cerling, 2002) and reconstructing paleoenvironments (Bocherens et al., 1996; Cerling et al., 2011; Kingston, 2007; Levin et al., 2008; Lüdecke et al., 2016; van der Merwe, 2013). Much of this work is accomplished through stable isotope analysis of enamel (Clementz, 2012; Kohn and Cerling, 2002; Lee-Thorp, 2008). In terrestrial animals, stable carbon isotopes of enamel bioapatite originally derive from the major groups of

* Corresponding author.
E-mail address: deming.yang@stonybrook.edu (D. Yang).

https://doi.org/10.1016/j.chemgeo.2020.119799
Received 15 April 2020; Received in revised form 24 July 2020; Accepted 26 July 2020
Available online 02 August 2020

consumed plants that use different photosynthetic pathways (*e.g.*, C_3 and C_4), which are isotopically distinct (Ambrose and DeNiro, 1986; Farquhar et al., 1989; Tieszen et al., 1979). Stable carbon isotope analysis of enamel confirmed that the majority of warthog diet is C_4 grass in the savanna ecosystem (Cerling and Harris, 1999; Harris and Cerling, 2002), but a diet consisting of C_3 grasses is also found at higher elevations (Levin et al., 2008; Teklehaimanot and Balakrishnan, 2017).

Stable oxygen isotopes in enamel bioapatite are ultimately sourced from the animal's body water, which is influenced by diet, physiology, and most importantly, water balance (Bryant and Froelich, 1995; Green et al., 2018a; Kirsanow and Tuross, 2011; Kohn, 1996; Levin et al., 2006; Longinelli, 1984; Luz et al., 1984). Because the water that an animal drinks derives from surface waters that are characterized by spatial and temporal variations in the local hydrological system (Bowen, 2008; Dansgaard, 1964; Gat, 1996), its body water also carries the environmental signal (Bryant and Froelich, 1995; Kohn, 1996; Longinelli, 1984; Luz et al., 1984). An important feature of mammalian enamel is that it is deposited incrementally and remains isotopically stable after formation (Balasse, 2002; Dean, 1987; Fricke and O'Neil, 1996; Simmer and Fincham, 1995). It preserves a record of the body water isotope condition for the duration of enamel formation, which typically spans a few months to several years in a tooth, depending on the species (Balasse, 2002; Kohn et al., 1998; Passey and Cerling, 2002; Uno et al., 2013). For this reason, intra-tooth isotope sampling in hypsodont herbivore teeth is a common technique to investigate environmental seasonality in archeological and paleontological research (Balasse et al., 2006; Bernard et al., 2009; d'Ambrosia et al., 2014; Frémondeau et al., 2012; Fricke et al., 1998; Fricke and O'Neil, 1996; Hartman et al., 2016; Higgins and MacFadden, 2009; Nelson, 2005; Reade et al., 2018; Reid et al., 2019; Roberts et al., 2018; Souron et al., 2012; Zazzo et al., 2002). However, any isotope sample taken from enamel integrates both the fast matrix secretion stage and the slow maturation stage of enamel mineralization (Balasse, 2002; Green et al., 2017; Passey and Cerling, 2002; Podlesak et al., 2008; Zazzo et al., 2010). The effects of this integration over different mineralization intervals are: 1) damping of the amplitude of the original body water and diet signal; and 2) distortion in the shape of the original signal (Green et al., 2018b; Passey and Cerling, 2002; Zazzo et al., 2005, 2010).

Mathematical models have been used to recover the unattenuated seasonal isotope variations in enamel or body water (Green et al., 2018b; Passey and Cerling, 2002; Passey et al., 2005a). The inverse model by Passey et al. (2005a) is most frequently used because it is easily adapted to most intra-tooth isotope profiles. It has three major assumptions: 1) the tooth grows at a constant rate; 2) enamel maturation starts immediately after initial matrix secretion; and 3) the maturation geometry is the same as the secretion geometry (Passey et al., 2005a). However, hypsodont molars that are commonly found in archeological or paleontological sites often follow a different mineralization pattern (Green et al., 2017, 2018b; Hoppe et al., 2004; Trayler and Kohn, 2017), which limits the use of the inverse model without modifications for molar maturation parameters. As a result, most intra-tooth isotope studies report the measured isotopic variation in enamel (*e.g.*, Balasse et al., 2006; Frémondeau et al., 2012; Higgins and MacFadden, 2009; Nelson, 2005), which only allows for qualitative interpretations of seasonality.

The common warthog is an ideal organism to investigate stable isotope variation in enamel for the purpose of environmental reconstruction because it has both continuously growing lower canines and hypsodont M3s. In this study, we first measured stable isotope intra-tooth profiles in two common warthog specimens. Second, to evaluate the assumptions of the inverse model (Passey et al., 2005a) on warthog teeth, we collected data on enamel growth and mineralization geometry in ever-growing canines and hypsodont M3s from three additional warthog specimens. Third, using the growth and mineralization parameters, we applied the inverse model to reconstruct the timeline of unattenuated seasonal $\delta^{18}O$ signal based on canine growth rates and canine intra-tooth $\delta^{18}O$ profiles. Fourth, we compared the unattenuated signal to measured isotope variation in M3s, to investigate how confidently the amplitude and duration of seasonality can be inferred from M3 intra-tooth profiles. Finally, we used this interpretive framework to investigate the duration of seasonality using published intra-tooth profiles of extant and archeological warthog M3s.

2. Materials and methods

2.1. Intra-tooth sampling of enamel and stable isotope analysis

Our warthog stable isotope samples originated from the Mpala Conservatory, Laikipia County, Kenya (latitude: 0.30°N; longitude: 36.88°E). A 17-year local precipitation record based on rain gauge readings (Caylor et al., 2019) indicates that the monthly precipitation distribution follows a bimodal pattern that is consistent with most of eastern Africa (Nicholson, 2018; Yang et al., 2015), with a long rainy season typically between March and June, and a short rainy season between October and November (Caylor et al., 2019). We sampled two warthog mandibles for intra-tooth stable isotope analysis. Both mandibles were at bone weathering stage 0–1, suggesting death occurred within the last few years before field collection (Behrensmeyer, 1978). To access the full length of enamel in both the canine and the M3, we extracted them from the left side of the mandible in each specimen. In both individuals, enamel formation in the cervical portion of the canines and M3s was still ongoing when the individuals died. The canines were sampled on the lingual side of the tooth. To access enamel in the M3s, the cementum cover was first removed (Fig. 1). Because the outer enamel surface on warthog M3s is rugose and intersects with inner

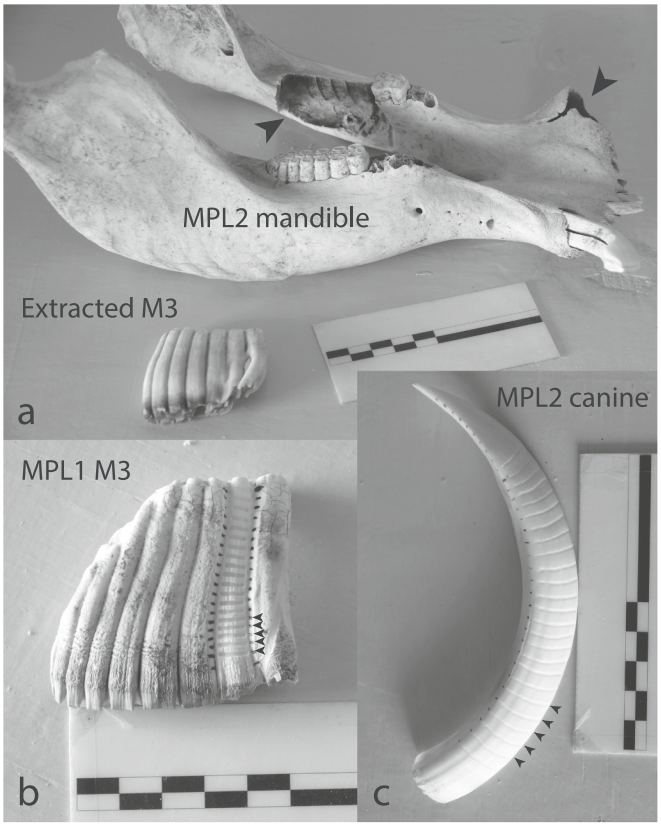

Fig. 1. Stable isotope sampling scheme; a) large arrow heads show where the canine and M3 were extracted from the left side of the MPL2 mandible; b) MPL1 lower left M3; small arrow heads show examples of sampling grooves on the lingual side of the second pair of pillars, after cementum is removed; c) MPL2 lower left canine; small arrow heads show sampling grooves on the lingual side of the canine; scale bar = 10 mm.

cementum, this layer (*ca.* 0.2 mm) was also removed to avoid possible contamination from cementum. Dentine and cementum samples were collected to evaluate the possibility of contamination (Supplementary S1). Intra-tooth sampling distance from the cervical margin was measured on the outer enamel surface. Bioapatite samples (including enamel, dentine, and cementum) were analyzed using standard phosphoric acid digestion with pretreatment (Cerling et al., 2015, Supplementary S1). All isotopic ratios are reported using per mil (‰) notation relative to the V-PDB standard, where $\delta^{13}C$ or $\delta^{18}O_{sample} = (R_{sample}/R_{standard} - 1) \times 1000$; and R_{sample} and $R_{standard}$ are the $^{13}C/^{12}C$ or $^{18}O/^{16}O$ ratios in the sample and standard for $\delta^{13}C$ and $\delta^{18}O$, respectively.

2.2. Enamel growth and geometry

Thin sections were made from three specimens of *Phacochoerus africanus*: 1) an upper right M3 (Souron1 specimen), 2) a lower right canine from a different individual (Souron2 specimen), and 3) an upper M3 (NKU specimen). Both Souron1 and Souron2 are specimens with no provenience information, which were donated to A. Souron as part of a laboratory collection. The upper M3 of the NKU specimen was collected by T. Cerling during the 1998 field season from Nakuru National Park, Kenya (latitude: 0.36°N; longitude: 36.10°E). The Souron1 specimen (M3) is slightly worn at the occlusal surface and enamel extension was still progressing at the cervical margin. In comparison, the NKU specimen is moderately worn, and the mesial root is fully formed. Because warthog M3s come into occlusion long before the roots are complete, using two M3 specimens at different wear stages allows us to nearly capture its entire growth trajectory. Because the Souron2 specimen (lower canine) is large and strongly curved, it was divided into four segments before longitudinal thin sections were prepared (Fig. 2a). The Souron1 specimen also displays a strong medio-lateral curvature and it was therefore transversely sectioned into two parts at about 60% of the crown height from the occlusal surface. Each part was then sectioned longitudinally along the second pair of pillars (Fig. 2b). The NKU specimen did not require division before making thin sections due to a lack of curvature on the second pair of pillars. We used upper molars because these were the only specimens available at the time. As there are no quantitative comparisons of the developmental patterns of upper *vs.* lower teeth in warthogs, we assumed that enamel extension rates in upper and lower molars are comparable. The thin sections were prepared at the target thickness of 100 μm, using the methods described in the Supplementary S1.

Thin sections were examined using a transmitted light microscope (Leica DM2500P) under plane polarized light. Digital images were taken with a Leica MC120HD camera using the Leica LAS software at the resolution of 1824 × 1368 pixels (1 pixel = 0.84 μm). Images were "photomerged" in Adobe Photoshop CS6 using the reposition function with the blend option selected. For each of the thin section montages, the enamel dentine junction (EDJ) was divided into deciles except for canine section 2, which was divided into 16 parts to accommodate for its particularly long EDJ. Daily incremental lines or laminations were counted within each decile (Fig. 2c and d). Appositional angles (or enamel formation front angles) were measured where daily laminations meet the EDJ using the angle arm tool in Photoshop CS6. Average enamel extension rates were calculated for each decile as the length of that segment of the EDJ divided by the number of daily increments in that decile (following Kierdorf et al., 2019). To account for the curvature in the canine, extension rates were corrected to the extension rate at the greater curvature of the canine where sampling distance was measured in intra-tooth profiles (Fig. 2a, Supplementary S2). Enamel daily secretion rates (DSRs) were also recorded using the same thin sections described above (detailed methods and results are reported in Supplementary S1). Both the buccal and lingual sides of the molar thin sections (Souron1 and NKU M3s) were imaged but data from the lingual sides are not reported due to lower visibility of enamel incremental lines.

2.3. Enamel mineralization geometry

Cervical portions of the canine (Souron2) and M3 specimens (Souron1 & NKU) were micro-CT scanned together to obtain enamel mineralization pattern. The specimens were scanned at PACEA/ University of Bordeaux with a General Electrics (GE) Vtome x|s X-ray

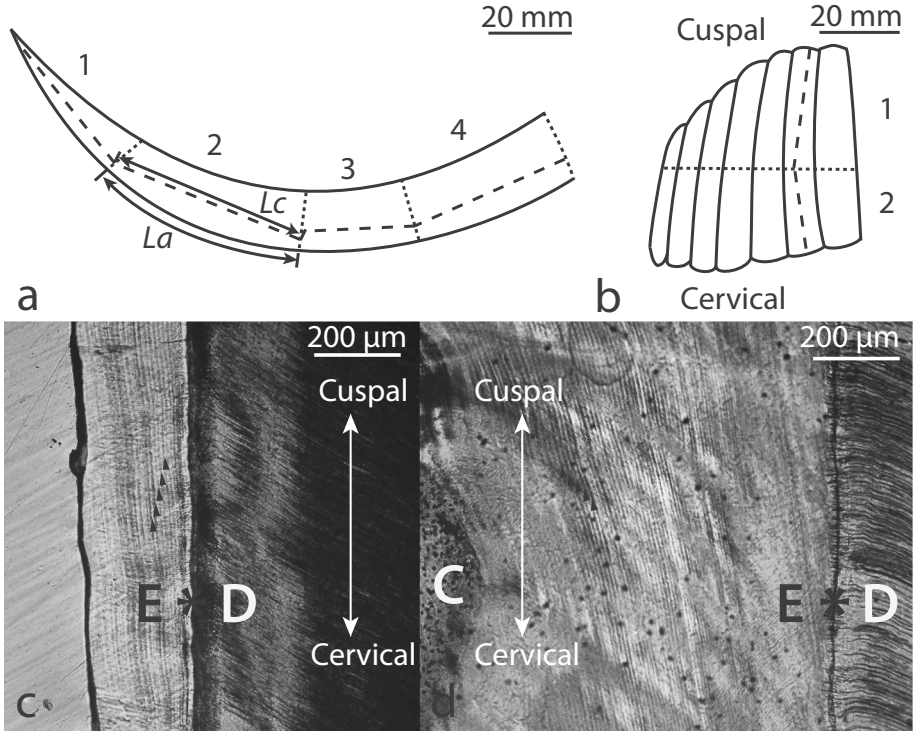

Fig. 2. Schematics of specimen preparation for thin sections and examples of microscopy images collected under transmitted light with polarization filter; a) preparation of the Souron2 specimen into four parts and enamel extension rate correction scheme; Lc = cord length; La = arc length; b) preparation scheme of the Souron1 M3 into two parts; dotted lines indicate sectioning planes of the general preparation stage; dashed lines indicate sectioning planes of the thin section stage; examples of thin section microscopy in c) the Souron2 canine, and d) the Souron1 third molar; small arrow heads indicate daily incremental lines or laminations in enamel; E = enamel; D = dentine; C = cementum; asterisk (*) = enamel-dentine junction.

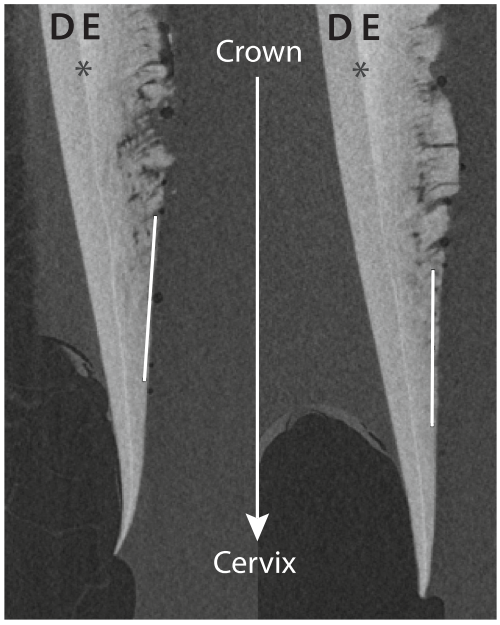

Fig. 3. Schematics of measuring relative density of immature enamel matrix from two separate slices of the micro-CT images of the Souron1 third molar specimen; in ImageJ, the transects (white lines) were drawn close to the enamel formation front while avoiding areas with high variability in grayscale values; D = dentine; E = enamel; asterisks (*) indicate the enamel-dentine junction, arrow indicates the direction of enamel extension.

microtomograph, at 120 kV and 200 μA settings with a tungsten target. A 0.1 mm copper filter was used to limit beam hardening effect. Reconstructions of the volumes were performed using the Datos|Acq software (GE), at the voxel density of 22.5 μm. Scan images were processed in AVIZO software to generate virtual sections longitudinal to the growth axis and perpendicular to the EDJ near the cervix for each tooth. Extracted images were imported to ImageJ, in which multiple transects were made to measure the grayscale values of different dental tissues: mature enamel, mature dentine, and immature enamel matrix at the molar enamel formation front (Fig. 3). Multiple transects were also made perpendicular to the EDJ, in order to capture relative density change of enamel along the EDJ referencing the geometry of the appositional front (Supplementary Figs. S1 and S2). For measuring relative density, average background value was subtracted from all measured grayscale values. Then all measured grayscale values were converted into fractions (0–1) of mature enamel, which is qualitatively defined as enamel that displays homogeneous grayscale values away from the cervix. Maturing enamel at different relative densities were mapped using the enamel matrix density as the baseline, and multiple density cutoffs at 0.1 increments, with mature enamel at the relative fraction of 1. To reduce false positives in this analysis, a 3-point median smoothing function was used in the grayscale values of the transects.

2.4. Intra-tooth stable isotope profiles and inverse modeling

After enamel growth, geometry, and mineralization patterns were obtained, we applied the inverse method developed by Passey et al. (2005a) to estimate the unattenuated isotopic amplitude to account for signal distortion due to enamel mineralization. Because the inverse model assumes a constant growth rate and mineralization geometry, it has mostly been used in continuously growing teeth. In this study, we used it in the canine profiles only (see Results section). This permits comparison between measured $\delta^{18}O$ in molar enamel and modeled $\delta^{18}O$ variation in canine enamel, which provides insights into the seasonal signal damping effect in molar enamel isotopic measurements. Detailed descriptions of the modeling method and parameters used are given in the Supplementary S1 and S2. A sensitivity test on the initial relative density of enamel matrix was performed and results are reported in Supplementary S1 and S2.

2.5. Statistics

Statistical analyses were performed in R (v. 3.6) (R Core Team, 2019). For pairwise comparisons, variables were first tested for normality using the Shapiro-Wilk test (Supplementary Table S1). Variables conforming to normality were tested with Welch's *t*-test. Otherwise, Mann-Whitney *U* test was used (Supplementary Table S2). For enamel extension rate estimates in both the warthog canine and M3s, ordinary linear regression models were used to produce the best fit line, with 95% Confidence Interval and 95% Prediction Interval for each model. We used ANCOVA to test whether there was a difference in the slopes of the linear models between the Souron1 and the NKU molars.

2.6. Isotope timeline reconstruction

Using the best fit extension rate estimates and their 95% Prediction Intervals to represent error estimates, we reconstructed the isotope timeline for both canine and M3 profiles using the sampling distance measurement. Due to the low variation in $\delta^{13}C$ profiles in both specimens (regardless of tooth type), we only report the results based on $\delta^{18}O$ measurements, which allow for interpretation of seasonal patterns. We first accounted for wear stages of the tooth by estimating the height of the crown that is missing at the occlusal surface. Then we used growth rate estimates and the corrected distance measurements to calculate the amount of time represented at each sampling interval. Finally, a timeline was reconstructed using a cumulative function and the sampling intervals (Fig. 4). For the M3 profiles, we assumed that the distance measurement at the outer enamel surface is the same at the EDJ where average enamel extension rates are collected.

After obtaining the reconstructed timelines, the inverse model output from canine data and the measured molar data were manually aligned at the most consistent data point of the two profiles. We used local high and low points in both canine model output and measured molar enamel $\delta^{18}O$ to interpret duration and amplitude of seasonality for the following reasons. First, seasonal changes in $\delta^{18}O$ of drinking water input and fraction of evaporative water output are buffered by the reservoir effect of the animal's body fluid (Bryant and Froelich, 1995; Cerling et al., 2007; Green et al., 2018a). While the water turnover rate of the common warthog is unknown, the differential ($d\delta^{18}O/dt$) of body water $\delta^{18}O$ input, for example, from a local low point to a high point is consistently positive, which corresponds to general dry season conditions (Green et al., 2018b; Kohn, 1996; Kohn et al., 1998). Second, local high and low points can be determined consistently without further assumptions. Therefore, we interpreted an interval with a steady increase in the $\delta^{18}O$ values (including a plateau if present) right before a significant decrease as the dry season, while an interval with the opposite pattern as the rainy season. Calculating signal attenuation effect in a molar profile relative to inverse model output based on the corresponding canine profile has the following sources of error: 1) uncertainty in the inverse model $\delta^{18}O$ output; and 2) uncertainty in the measured enamel $\delta^{18}O$. We propagated these sources of error as the square root of the sum of squares.

3. Results

3.1. Intra-tooth stable isotope profiles

For MPL1, 19 samples each were analyzed for the canine and the M3. For MPL2, 25 and 19 samples were analyzed for the canine and the M3, respectively (Table 1). The $\delta^{13}C$ values of MPL1 range between −1.8‰ and 2.2‰, which are overall similar to those of MPL2, between −1.6‰ and 1.5‰ (Fig. 5). The $\delta^{18}O$ values of MPL1 range between

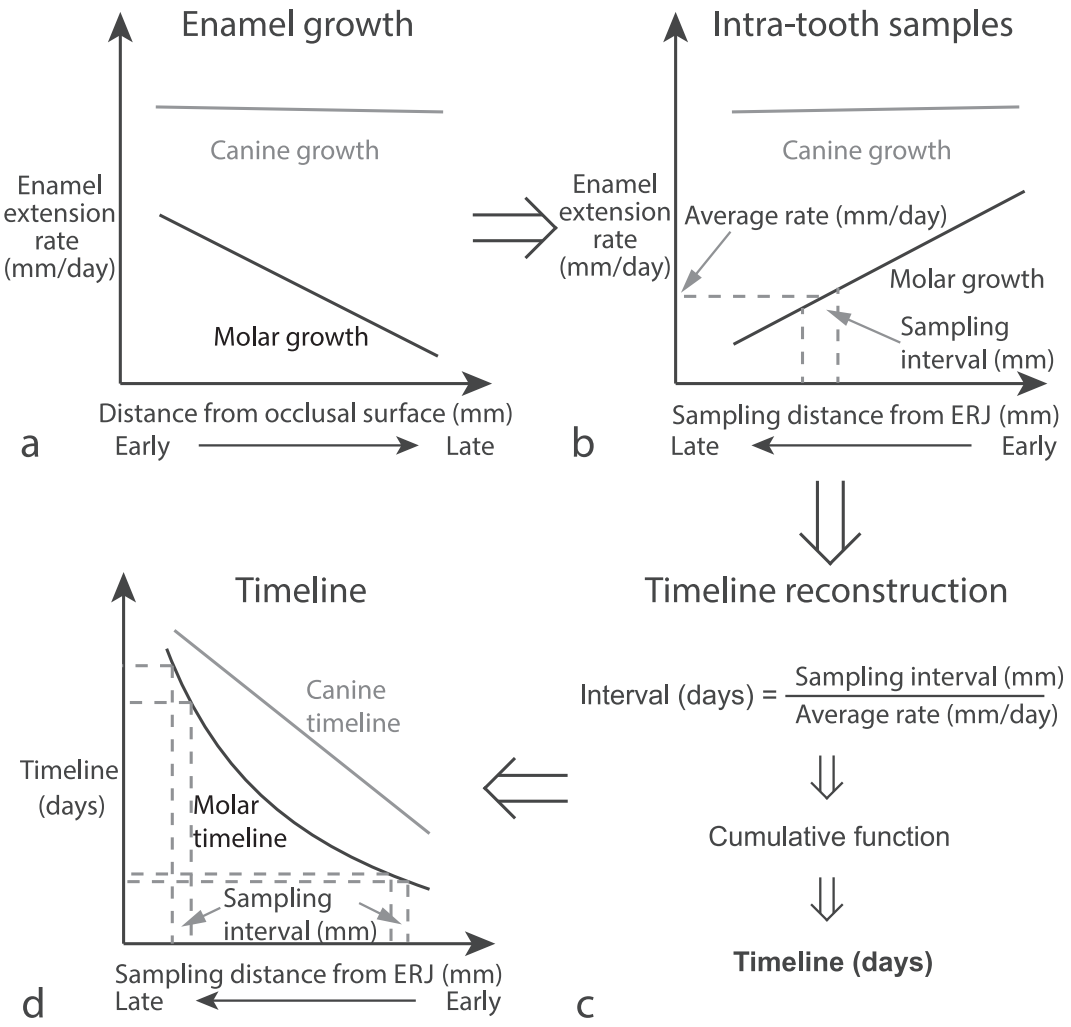

Fig. 4. Schematics of timeline reconstructions using extension rate estimates and intra-tooth sampling distance measurements in warthog canines and molars; note that sampling distance, as in b) from cervical to occlusal, is measured in the opposite direction as enamel growth as in a) from occlusal to cervical; arrow directions below the x-axes indicate the dental developmental sequence from early to late development; d) shows the effect of a decreasing growth rate in molars: the same sampling interval in a later stage of dental development corresponds to a longer time interval along the timeline; in comparison, a near constant growth rate in the canine corresponds to evenly spaced intervals along a linear timeline; ERJ = enamel-root junction (or cervix).

2.3‰ and 7.1‰, which are about 1‰ higher than those of MPL2, between 1.2‰ and 5.8‰ (Fig. 5). The $\delta^{13}C$ and $\delta^{18}O$ values of both MPL1 and MPL2 fall largely within the range of extant *Phacochoerus* spp., reported in Harris and Cerling (2002). However, the mean $\delta^{13}C$ values between the canines and the M3s in both MPL1 and MPL2 are significantly different ($p < 0.001$, Fig. 5c, Supplementary S1), while the mean $\delta^{18}O$ values between the canine profile and the M3 are significantly different in MPL1 ($p < 0.01$), but not in MPL2 ($p = 0.6$, Supplementary S1). The difference in $\delta^{13}C$ values between the canine and M3 means is 2.4‰ in MPL1 and 2.0‰ in MPL2. We use the Δ notation and the following equation $\Delta_{c\text{-}m}{}^{13}C = \delta^{13}C_c - \delta^{13}C_m$ to describe this isotopic spacing between canine and molar enamel bioapatite. The average $\Delta_{c\text{-}m}{}^{13}C$ of the two specimens is 2.2 (± 0.2) ‰. To put this difference in the context of dietary reconstruction, we calculated the nominal percentage of C_4 plants (%C_4) in diet (Table 2) using modal $\delta^{13}C$ values of C_3 and C_4 plants in linear mixing models (detailed methods see Supplementary S1). A 2‰ difference in $\delta^{13}C$ can translate into a 14% difference in dietary C_4 (Table 2). The $\delta^{13}C$ and $\delta^{18}O$ values

Table 1
Summary of $\delta^{13}C$ and $\delta^{18}O$ values of canine and third molar (M3) profiles of MPL1 and MPL2; all results are reported relative to the Vienna Pee Dee Belemnite (V-PDB) standard.

Specimen (number of samples)	Profile	Mean (‰)	1σ (‰)	Median (‰)	Minimum (‰)	Maximum (‰)
MPL1 canine (19)	$\delta^{13}C$	1.6	0.4	1.6	0.8	2.2
	$\delta^{18}O$	5.2	1.1	5.1	2.4	7.1
MPL1 M3 (19)	$\delta^{13}C$	−0.8	0.5	−0.7	−1.8	−0.1
	$\delta^{18}O$	4.1	1.0	3.9	2.3	5.7
MPL2 canine (25)	$\delta^{13}C$	0.8	0.3	0.7	0.3	1.5
	$\delta^{18}O$	4.0	1.4	4.2	1.2	5.8
MPL2 M3 (19)	$\delta^{13}C$	−1.2	0.2	−1.2	−1.6	−0.9
	$\delta^{18}O$	3.8	0.9	3.9	2.0	5.5

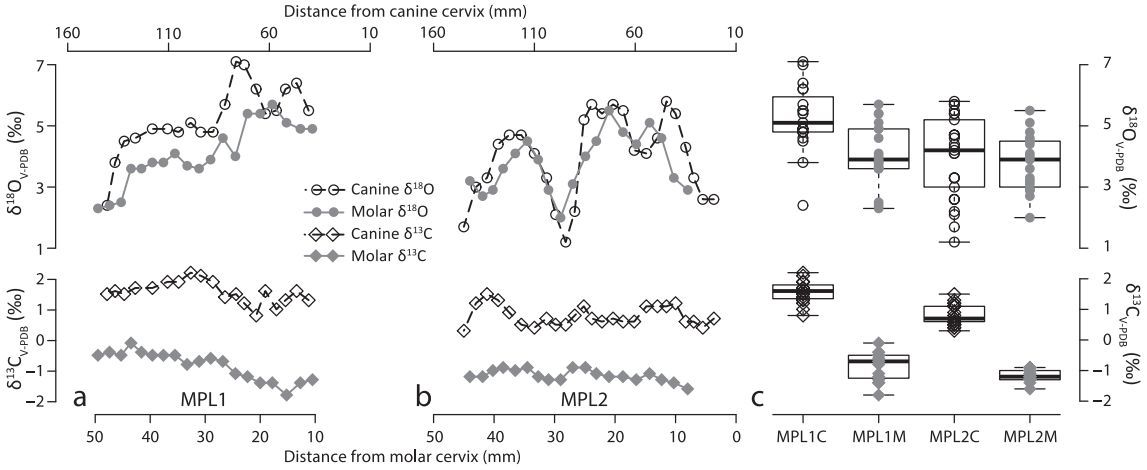

Fig. 5. Intra-tooth stable isotope variation in $\delta^{18}O$ and $\delta^{13}C$ in a) MPL1 lower canine and lower third molar; and b) MPL2 lower canine and lower third molar; c) comparison in the distribution of the isotope profiles; boxes indicate inter-quartile ranges; and whiskers indicate 95% confidence intervals, or the minimum-maximum range when no outlier is identified; thick lines indicate medians; upper section of the figure shows $\delta^{18}O$ values; lower section of the figure shows $\delta^{13}C$ values; open symbols with dashed lines represent canine profiles; filled symbols with solid lines represent third molar profiles; $\delta^{18}O$ distributions in the canines and molars are highly similar while there is an offset observed between tooth types in $\delta^{13}C$; the patterns of seasonal variation observed in $\delta^{18}O$ in the two teeth of the same individual are quite similar; MPL1C = MPL1 lower canine; MPL1M = MPL1 lower third molar; MPL2C = MPL2 lower canine; MPL2M = MPL2 lower third molar; V-PDB = Vienna Pee Dee Belemnite.

Table 2
Isotopic spacing between canine and M3 enamel median $\delta^{13}C$ values ($\Delta_{c\text{-}m}{}^{13}C$) and corresponding difference in nominal $\%C_4$ in diet. Upper and lower values in $\Delta\%C_4$ were calculated using different linear mixing lines (Supplementary S1).

Specimen	Tooth	Mean $\delta^{13}C$ (‰)	$\Delta_{c\text{-}m}{}^{13}C$ (‰)	$\Delta\%C_4$ diet (range)
MPL1	Canine	1.6	2.4	16 (14–21)
	M3	−0.8		
MPL2	Canine	0.8	2.0	14 (12–17)
	M3	−1.2		

of the profiles are reported in Supplementary S2.

3.2. Warthog canine and M3 enamel growth rate estimates using thin sections

For the Souron2 lower canine, the majority of the daily enamel extension rates fall between 0.2 and 0.3 mm/day (Fig. 6a). There is a non-significant trend of rate decrease (p-value = 0.197) as canine growth progresses towards the cervical margin (Table 3). In both the Souron1 and the NKU M3s, there is a significant linear decrease in the extension rates (Fig. 6b; Table 3). There is no difference between the slopes of the two M3 linear regressions (p-value = 0.817). Molar daily enamel extension rates fall between 0.03 and 0.12 mm/day (Fig. 6b). In general, at the greater curvature, canines grow 2 to 10 times faster than M3s.

3.3. Warthog M3 and canine enamel maturation pattern

Based on micro-CT grayscale values, the initial M3 enamel matrix after secretion has a relative density of 0.47 compared to average fully mineralized molar enamel (Table 4; Supplementary S1). The maturing enamel increases its density soon after apposition, especially for the portion closest to the EDJ (innermost enamel). The innermost enamel remains in higher relative density than both middle and outer enamel during the maturation process. Due to cementum formation at the outer enamel surface soon after apposition, relative density of outer enamel is lower at *ca.* 8 mm from the cervix (Fig. 7b). As relative density increases, the reconstructed M3 mineralization fronts show a substantial increase in the angle by *ca.* 23° from the appositional front, at *ca.* 11°

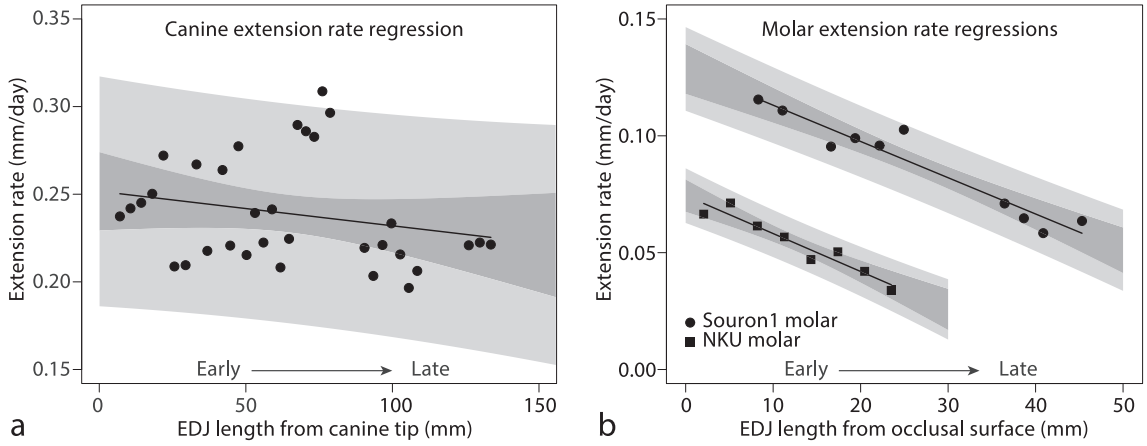

Fig. 6. Daily enamel extension rate measurements along the EDJ in a) Souron2 lower canine enamel, and b) third molar enamel; black circles: Souron1 M3 extension rates; black squares: NKU M3 extension rates; dark gray shaded area: 95% confidence interval for the best fit lines; light gray shaded area: 95% prediction intervals for the regression models; arrow directions below the x-axes indicate the dental developmental sequence from early to late development.

Table 3
Canine and molar extension rate ordinary linear regression statistics; CI = confidence interval; s.e. = standard error.

	Adjusted R^2	Intercept [95% CI]	*p*-value	Slope [95% CI]	*p*-value	Residual s.e.
Souron2 (Canine)	0.0225	0.252 [0.229–0.274]	< 0.001	-1.97×10^{-4} [$(-5.0$ to $1.08) \times 10^{-4}$]	0.197	50.4%
Souron1 (M3)	0.913	0.129 [0.118–0.139]	< 0.001	-1.55×10^{-3} [$(-1.92$ to $-1.19) \times 10^{-3}$]	< 0.001	0.6%
NKU (M3)	0.908	0.0744 [0.0675–0.0813]	< 0.001	-1.62×10^{-3} [$(-2.10$ to $-1.15) \times 10^{-3}$]	< 0.001	0.4%

the EDJ, to the 0.95 density line, at *ca.* 34°.

For the Souron2 lower canine, the cervical most portion of the immature enamel matrix was not preserved during the preparation process of the specimen (Fig. 7a; Supplementary Fig. S1), likely due to the thinness of canine enamel (~200 μm, from thin sections). Since there is no substantial change in the appositional angle of the canine enamel along the growth axis (Supplementary Fig. S4), estimates of the outline of immature enamel matrix was made using the average appositional angle of 2.5°, and the distance between the tip of the dentine forming front and the preserved edge of canine enamel. Because this portion of immature enamel matrix is not preserved, we assume that the initial matrix density is the same as in the molar enamel matrix, which has a relative density of 0.45 compared to average fully mineralized canine enamel (Table 4; Supplementary S1). As relative density increases, the reconstructed canine mineralization fronts show a gradual increase in the angle in the canine specimen, from the reconstructed appositional front, at *ca.* 2.5° to the EDJ, to the 0.95 density line, at *ca.* 6.2° (Fig. 7a).

3.4. Estimating unattenuated $\delta^{18}O$ signal using inverse modeling of canine profiles

The inverse model $\delta^{18}O$ output for the canine profiles is interpreted to represent the unattenuated $\delta^{18}O$ signal in enamel. Model output results are presented as the mean profile of 100 model solutions. The modeled profile for MPL1 has minimum and maximum values of 1.9‰ and 7.6‰, respectively (Fig. 8). The modeled profile for MPL2 has minimum and maximum values of 0.8‰ and 6.7‰, respectively. The amplitudes between the modeled minimum and maximum values for MPL1 and MPL2 are 5.7‰ and 5.9‰, respectively. The mean ± 2σ of the 100 iterations of model output for both MPL1 and MPL2 canine profiles are shown graphically in Fig. 8. The measured canine enamel $\delta^{18}O$ values follow the shape of mean model output in both specimens very well. The signal amplitude of measured canine profiles is on average 80% of the amplitude of model output, assuming that it represents the full range of unattenuated seasonal $\delta^{18}O$ signal.

3.5. Timeline reconstruction and $\delta^{18}O$ signal damping in M3 profiles

There is substantial overlap between the reconstructed timelines of molar $\delta^{18}O$ profiles and unattenuated canine profiles produced by the inverse model (Fig. 9a and b). Although the shapes of the curves in each specimen are similar, the amplitude of isotopic change is much smaller in the molar profiles. When comparing individual rainy and dry seasons based on local high and low $\delta^{18}O$ values (Fig. 9c and d), there is a discrepancy between the timeline of model reconstructed isotopic input and the M3 timeline, in that only two out of ten (20%) of the interpreted seasonal intervals (where D = dry and R = rainy) in the M3 timeline are consistent with unattenuated canine timeline (Supplementary Table S3). In contrast, when interpretations are based on the entire seasonal cycle (D + R), the consistency improves substantially in that six out of eight cycles (75%) are consistent between the M3 timeline and the canine timeline (Table 5). The interpreted seasonal cycles have a maximum of 235 days and a minimum of 97 days. Using local high and low $\delta^{18}O$ values (per season), M3 isotope profiles preserve on average 50% of the $\delta^{18}O$ signal amplitude of unattenuated canine profiles (50% signal reduction), with an average uncertainty of 17%. If full range of the profiles is used, this estimate is higher, at 60% of the variation, corresponding to a 40% signal reduction, and at a lower uncertainty of 9% (Table 6).

4. Discussion

4.1. Enamel histology

The geometry and extension rates of warthog canine and M3 enamel allow for estimation of the amount of time represented in canine and molar isotope profiles. It might be intuitive that the lower canine is the longer tooth (often over 150 mm), and therefore might preserve a longer record of body water chemistry than the M3s (often under 50 mm). Our results show that the M3s can preserve up to 1.5 years of isotope record, which is not much shorter than the corresponding lower canine (Fig. 9). This is consistent with previous observations in warthog dental ontogeny (Mason, 1984), and the estimate that *ca.* 1.5–2 years of isotope record can be obtained from warthog M3s (Reid et al., 2019). The two M3s (Souron1 and NKU) of different wear stages have shown the same pattern of rate decrease as enamel extends towards the cervical margin. The regressions have high R^2 values and low residual standard errors (Table 3), which indicates that the linear models can provide reliable estimates for M3 enamel extension rates based on crown height measurements. Non-linear decrease in enamel extension rates of herbivore molar enamel has been observed in other studies (Bendrey et al., 2015; Kierdorf et al., 2013; Zazzo et al., 2012) and modeled using the cumulative daily incremental markings and EDJ length (Green et al., 2017). We did not use this method because our enamel geometry data is based on one or two specimens, in which independence between cumulative data points cannot be assumed.

Table 4
Average relative density measurements of canine and molar dental tissue based on micro-CT scan grayscale values (16-bit); all grayscale values are corrected for background noise (air density = 0 relative density). Because the immature canine enamel matrix is not preserved in the specimen, the initial density is assumed to have the same grayscale value as immature molar enamel, which is marked with an asterisk (*).

	Mature molar enamel	Molar dentine	Molar enamel matrix	Mature canine enamel	Canine dentine	Canine enamel matrix
Grayscale value (1σ)	45,073 (2,059)	28,259 (2,454)	21,351 (3,793)	47,649 (1,622)	26,816 (1,562)	*21,351 *(3,793)
Relative density (1σ)	1 (0.05)	0.63 (0.05)	0.47 (0.08)	1 (0.03)	0.56 (0.03)	*0.45 *(0.08)

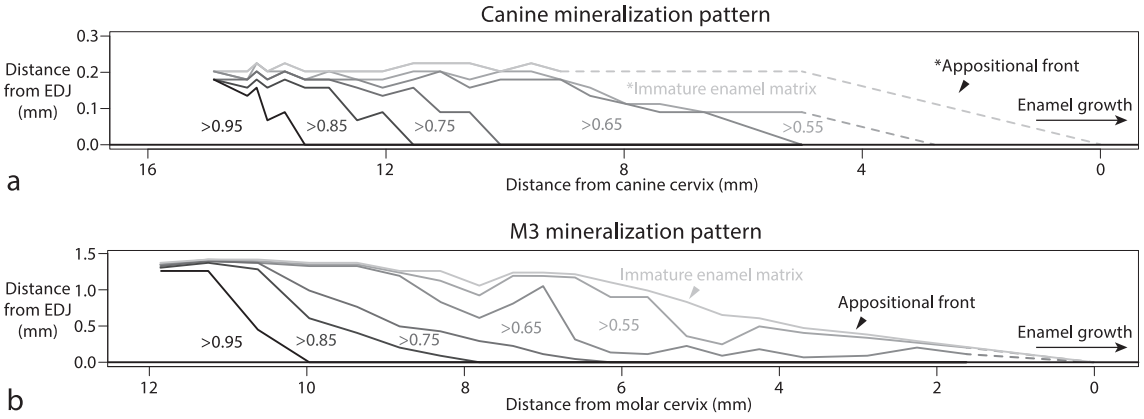

Fig. 7. Reconstructed enamel mineralization geometry based on micro-CT grayscale comparison in a) Souron2 lower canine and b) Souron1 M3; note the difference in the range of y axis between the two plots, indicating much thinner enamel in the canine; the apparent angles of apposition/mineralization are not to scale; the appositional front of immature canine enamel in a) is reconstructed based on the preserved EDJ and the average appositional angle of 2.5°, which is marked with an asterisk (*).

Furthermore, linear models for extension rates not only require fewer parameters, but also match our extension rates with high R^2 values of the regressions. Our timeline reconstructions depend on the assumptions that extension rates are the same between buccal and lingual sides of the crown, between mesial and distal pillars, and between upper and lower M3s. We are confident in the extension rates of the buccal second pillar of upper M3s, but the rates could vary between buccal and lingual sides of the tooth (Kierdorf et al., 2019). Future studies that evaluate growth rates in other molar crown regions (*e.g.*, lingual, mesial, distal) will help to improve the application of our methods to intra-tooth isotope profiles.

The insignificant decline in canine extension rate as enamel grows closer to the cervical margin is consistent with the assumption that the lower canine is an ever-growing tooth. However, there are two limitations that are associated with the canine extension rate estimates. First, a large amount of variation in the measured enamel extension rates is not accounted for in the linear model (R^2 = 0.02), which explains the uncertainty associated with our timeline reconstructions. Second, our canine growth rate estimates are based on one specimen (Souron2 canine) only. Warthog upper canines show different growth trajectories in males and females after 19–20 months of age (Mason, 1984). This sexual dimorphism may also influence the lower canines. We do not have sufficient information on the sex of the specimens that have been analyzed. However, the independently reconstructed canine and M3 timelines have significant overlap in both MPL specimens, which grants credibility to our methods. Future studies that specifically focus on sexual dimorphism in canine growth trajectories will provide valuable information.

4.2. Enamel maturation patterns

The enamel maturation pattern in the warthog canine is overall consistent with the model assumption that maturation begins almost immediately after secretion of enamel matrix in ever-growing teeth such as canines of the hippopotamus (Passey and Cerling, 2002). While the gradual increase in the angles of mineralization fronts is inconsistent with the model assumption that maturation occurs at the same angle to the EDJ as the apposition angle, we assume that it has minimal effects on the modeling results due to consistently low mineralization angles, thin enamel, and relatively large sampling intervals (~5 mm). The M3 shows a different pattern: apposition begins at a low angle relative to EDJ, while maturation occurs at a much higher angle as enamel density increases (Fig. 7), and the innermost enamel shows higher relative density. This pattern is consistent with what is observed in other hypsodont mammals (Blumenthal et al., 2014, 2019; Green et al., 2017; Hoppe et al., 2004; Trayler and Kohn, 2017). The high mineralization angles, relatively thick enamel, and small sampling intervals are the main reasons why we did not use the inverse model in the M3 profiles. A new mathematical model that takes the molar mineralization pattern into account may be applicable to suid molars (Green et al., 2018b), but is not yet easily implemented. Our dataset potentially allows for comparison of isotope timelines that are independently reconstructed based on different models and different tooth types in the future, which might improve our understanding of the assumptions in the enamel mineralization process.

Our dental tissue density measurements are based on grayscale values of micro-CT scans. Micro-CT may not the best method to

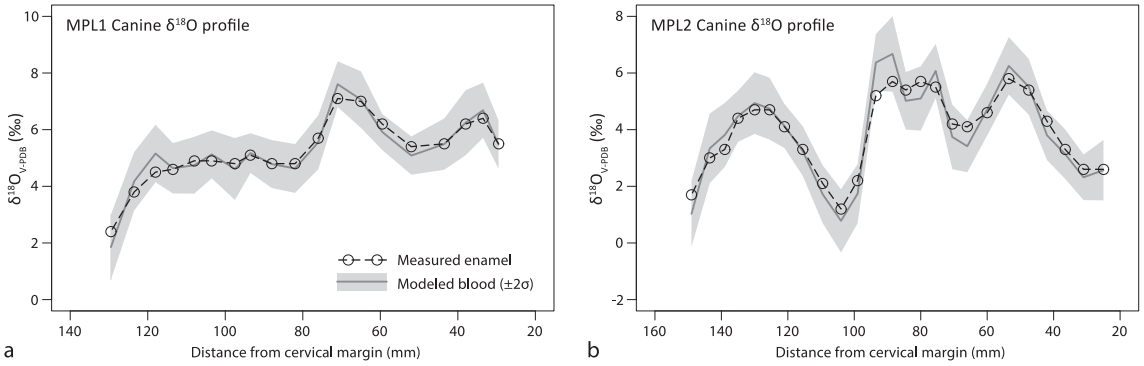

Fig. 8. Intra-tooth $\delta^{18}O$ profiles of warthog canines (MPL1 and MPL2); open circles and dashed lines are measured data; the thick line is the mean of 100 inverse model solutions for the estimated initial $\delta^{18}O$ variation in enamel (modeled); shaded area is ± 2σ of the solutions; V-PDB = Vienna Pee Dee Belemnite.

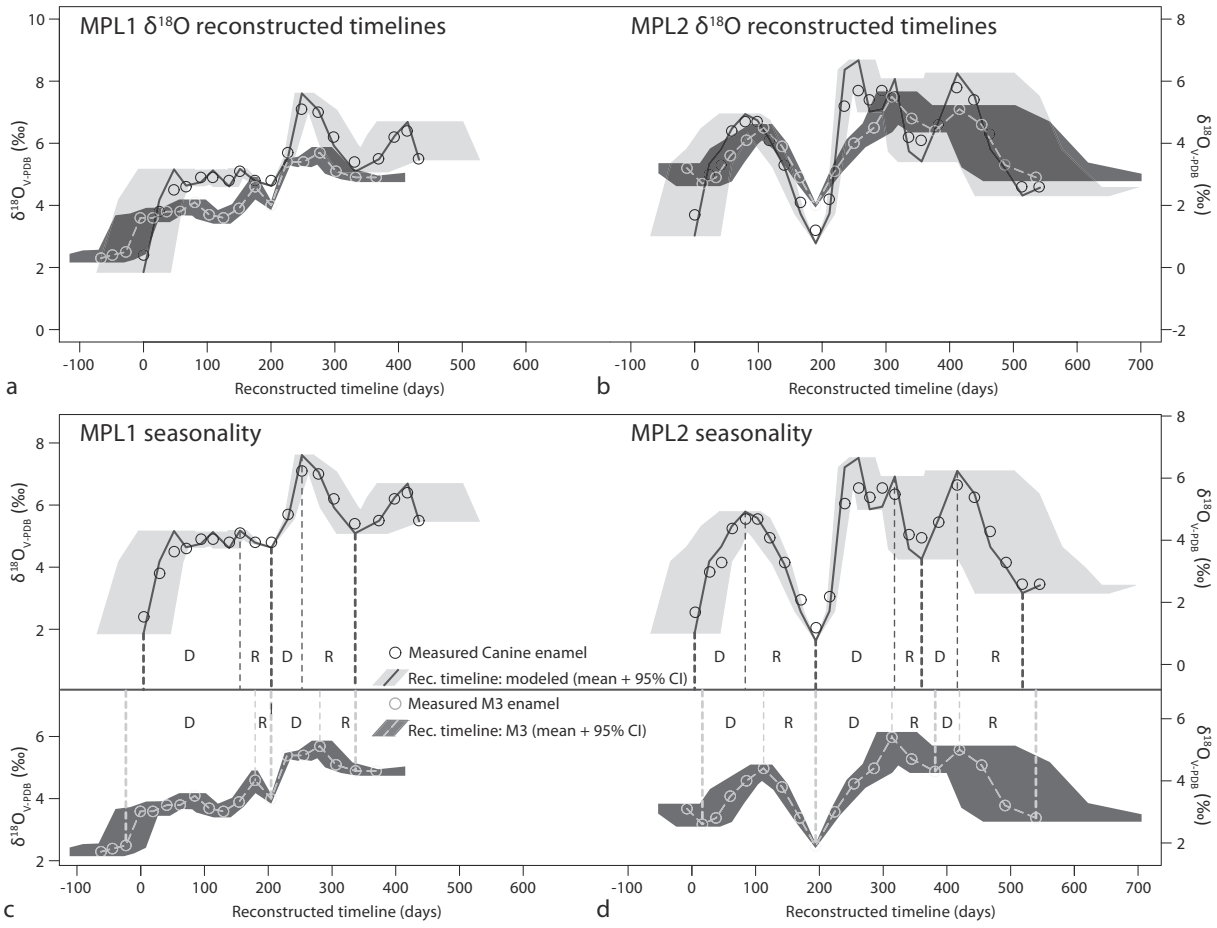

Fig. 9. Comparison of reconstructed timelines of M3 (using M3 extension rates) to modeled unattenuated canine $\delta^{18}O$ in a) MPL1 and b) MPL2 specimens; open circles are measured enamel $\delta^{18}O$ in the M3s; gray dashed line with dark gray shading is the reconstructed timeline (mean + 95% confidence interval) using M3 extension data; black solid line with light gray shading is the reconstructed timeline (mean + 95% confidence interval) of mean inverse model solutions (modeled $\delta^{18}O$, as in Fig. 8), using canine enamel extension rate data; because the timelines were reconstructed cumulatively using interval estimates, the errors are larger towards the ends of the profile than the middle of the profile; Rec. = reconstructed; CI = confidence interval; V-PDB = Vienna Pee Dee Belemnite; D = dry season; R = rainy season.

Table 5
Durations of seasonal cycles, in days, interpreted from unattenuated canine timelines and M3 timelines in Fig. 9, using the sum of one rainy season and one dry season in no particular order; best fit durations that are within the ± 15% limit between the unattenuated canine timelines and the molar timelines are considered consistent and bolded; the ± 15% limit serves as a more conservative threshold for evaluating the duration estimates, compared to the range; durations of seasonal cycles are also reported using precipitation record at Mpala, Laikipia (Caylor et al., 2019, more details in Supplementary S1); asterisks (*) indicate that timeline reconstruction was based on the inverse model output of canine isotope profiles.

	MPL1 Canine*	MPL1 M3	MPL2 Canine*	MPL2 M3	Mpala rainfall record
Season	–	–	Dry + Rainy	Dry + Rainy	Dry + Rainy
Duration [range] (days)	–	–	**190** **[150–258]**	**186** **[156–231]**	171 [82–248]
Season	–	–	Rainy + Dry	Rainy + Dry	Rainy + Dry
Duration [range] (days)	–	–	235 [184–323]	202 [164–264]	212 [120–259]
Season	Dry + Rainy	Dry + Rainy	Dry + Rainy	Dry + Rainy	Dry + Rainy
Duration [range] (days)	**201** **[159–273]**	**228** **[197–271]**	166 [130 − 232]	195 [153–270]	206 [113–243]
Season	Rainy + Dry	Rainy + Dry	Rainy + Dry	Rainy + Dry	Rainy + Dry
Duration [range] (days)	**97** **[76–134]**	**102** **[85–126]**	**98** **[76–139]**	**110** **[82–165]**	163 [97–240]
Season	Dry + Rainy	Dry + Rainy	Dry + Rainy	Dry + Rainy	Dry + Rainy
Duration [range] (days)	**131** **[102–184]**	**132** **[109–167]**	**158** **[121–228]**	**155** **[112–253]**	171 [82–248]

Table 6
Summary of calculated percentage signal preserved and associated uncertainty in warthog M3s based on reconstructed timelines of inverse model output (canine) and molar enamel measurements.

	Average % signal preserved (# of seasonal intervals)	Damping effect (per season)	Uncertainty (± 1σ)	% signal preserved based on total $\delta^{18}O$ range	Damping effect (total $\delta^{18}O$ range)	Uncertainty (± 1σ)
MPL1	60% (n = 4)	40%	20%	60%	40%	9%
MPL2	49% (n = 6)	51%	16%	59%	41%	8%
Combined	50% (n = 10)	50%	17%	60%	41%	9%

investigate absolute mineral density due to well-known issues such as beam hardening (Kovács et al., 2009; Zou et al., 2011). Schmitz et al. (2014) reported slightly higher estimates in enamel mineral density using micro-CT compared to ashing and scanning electron microscope (BSE-SEM), but the estimates of micro-CT still correspond well with the other methods. With this caveat, our measured relative density fraction of immature enamel matrix is 0.47 for the M3, corresponding to 0.45 for the canine (Table 4), which is likely an overestimate of the true value. This fraction is significantly higher than reported initial mineral fractions of rodent, equid, and hippopotamus enamel matrix, at *ca.* 0.25 (Blumenthal et al., 2014; Passey and Cerling, 2002; Schmitz et al., 2014), but lower than that for elephants (*ca.* 0.65) determined by similar micro-CT methods (Uno et al., in press). To investigate the extent to which our interpretations could be affected by this potential overestimation, we conducted a sensitivity test using different mineral fraction values in the MPL2 dataset (Supplementary S1). The results show slightly different attenuation effects between the trials (Supplementary Fig. S3), but they are nonetheless very similar to the pattern reported in Fig. 8. A previous study investigating *Equus* enamel and dentine density based on BSE-SEM reported a dentine mineral fraction of *ca.* 0.6 of fully mineralized enamel (Blumenthal et al., 2014). This value is similar to our reported molar dentine (0.63 ± 0.05) and canine dentine (0.56 ± 0.03) values (Table 4), indicating that our density measurements are at least within a reasonable range.

Our results suggest that enamel extension and mineralization paramaters are essential in timeline reconstructions and mathematical modeling to reconstruct the unattenuated isotopic signal. Enamel extension rate patterns of fossil equid teeth are available in multiple datasets (Nacarino-Meneses et al., 2017; Orlandi-Oliveras et al., 2019), which can offer more information on existing intra-tooth isotope profiles. However, enamel mineralization patterns in fossil herbivore teeth could be difficult to obtain using conventional methods such as SEM and micro-CT. New methods such as elemental distribution (*e.g.*, Dean et al., 2019; Müller et al., 2019) may offer further insights into enamel mineralization processes of extinct taxa.

4.3. Warthog intra-tooth profiles: difference between canine and molar enamel

The consistent isotopic spacing ($\Delta_{c\text{-}m}{}^{13}C$ = 2.2 ± 0.2‰) between the canine and the M3 profiles is surprising. Because the warthog M3 has thick cementum cover at the outer enamel surface, and the canine enamel is very thin, contamination from associated cementum and/or dentine is a possible explanation. However, after measuring both dental tissues from MPL1 for carbon isotope ratios, this possibility is eliminated based on the data and reasoning outlined in Supplementary S1. A smaller spacing (*ca.* 1‰) between canine and incisor enamel is also present in domestic pigs (Frémondeau et al., 2012), but was not discussed by the authors (see Supplementary S1). Previous studies that investigate the isotopic enrichment factor (ε^* notation, see Supplementary S1 for definition) between diet and bioapatite often assume a single value within a mammalian species (*e.g.*, Cerling and Harris, 1999; Passey et al., 2005b; Sponheimer et al., 2003; Tejada-Lara et al., 2018). Our observed $\Delta_{c\text{-}m}{}^{13}C$ suggests the possibility that different enrichment factors are associated with the two tooth types, respectively, within a single species. This value is similar to or greater than the difference in the enrichment factors between herbivores with different body masses, and between some foregut and hindgut fermenters (Cerling and Harris, 1999; Passey et al., 2005b; Tejada-Lara et al., 2018). These observations suggest caution when comparing stable carbon isotope results between enamel of suid canines and other tooth types, as it may introduce discrepancy in dietary interpretations (Table 2). This caution may also extend to comparing carbon isotope results from morphologically divergent tooth types in other mammalian taxa. Future studies that quantify the isotopic enrichment factors in different tooth types will help to resolve the observed $\Delta_{c\text{-}m}{}^{13}C$.

Despite the $\Delta_{c\text{-}m}{}^{13}C$ within the same individual, the $\delta^{18}O$ profiles overall show good agreement between molars and canines in absolute values and pattern. Based on the reconstructed timelines of the $\delta^{18}O$ profiles (Fig. 9), the canine and M3 timelines in MPL2 represent nearly the same amount of time. However, there is larger temporal offset between the canine and M3 timelines in MPL1: the beginning of the M3 timeline is likely not captured by the canine; and the end of the canine timeline is likely not captured by the M3. If we assume that this offset can entirely account for the difference observed in MPL1, the question of why there is a difference in $\delta^{13}C$ and not $\delta^{18}O$ between the two tooth types is puzzling.

The most fundamental difference between canine and molar enamel is that the canine enamel is much thinner than that of the M3s, which results in different mineralization geometry and corresponds to faster growth and mineralization rates. This difference in the mineralization geometry could be the primary source of the difference in $\delta^{13}C$ mentioned above. Enamel mineralization has two distinct stages: the secretion stage involves the production of a partially mineralized enamel matrix; the maturation stage involves the removal of organics and water from the matrix, and the incorporation of new mineral ions into the hydroxylapatite crystals (Robinson et al., 1979; Simmer and Fincham, 1995; Suga, 1982). In both stages, carbonate ions are incorporated into hydroxylapatite (Bronckers, 2017; Simmer and Fincham, 1995). It has been assumed that intercellular bicarbonate ions, which are the source of enamel carbonate, are in constant equilibrium with dissolved inorganic carbon (DIC) in the blood (Passey et al., 2005b; Podlesak et al., 2008), which is presumably in constant equilibrium with blood water (Green et al., 2018a). However, our results suggest that the situation may be more complicated. There are multiple steps in which equilibrium or kinetic fractionation could occur in the isotopic exchange between blood water and DIC (including carbonic acid, bicarbonate and carbonate ions) under potentially different pH and temperature conditions between the tooth types (Beniash et al., 2009; Damkier et al., 2014; Josephsen et al., 2010; Romanek et al., 1992; Volchansky et al., 1985). The mechanism of these complex processes, specific conditions, and apparent fractionations are beyond the scope of this study.

Enamel bioapatite consists of $Ca_{10}(PO_4)_6(OH)_2$ mineral with carbonate ($CO_3{}^{2-}$) substitutions in the phosphate ($PO_4{}^{3-}$) and hydroxyl (OH^-) sites (Elliott, 2002). Previous studies that focused on the relationship between oxygen isotope compositions of structural carbonate ($\delta^{18}O_C$) and phosphate ($\delta^{18}O_P$) components of enamel bioapatite suggest that both are reliable proxies for blood water $\delta^{18}O$ (Bryant et al., 1996; Chenery et al., 2012; Iacumin et al., 1996; Pellegrini et al., 2011). However, the fractions of mineral contribution to fully mineralized

bioapatite in the distinct stages of enamel mineralization differ between the two components: phosphate has a higher mineral contribution during the maturation stage than carbonate (Robinson et al., 1979; Sydney-Zax et al., 1991; Trayler and Kohn, 2017). Trayler and Kohn (2017) proposed that oxygen isotope resetting occurs during the maturation stage in enamel phosphate, which supports a simple intra-tooth isotope sampling strategy. This is later discussed by Green et al. (2018b), who supported an oxygen isotope exchange process in enamel phosphate during the maturation stage. If oxygen isotope exchange/resetting occurs in the phosphate component, a similar process may also occur in the carbonate component, which potentially explains why there is no consistent baseline difference in $\delta^{18}O_C$ between canine and molar enamel. On the other hand, the $\Delta_{c\text{-}m}{}^{13}C$ suggests different mechanisms in which water and DIC (*e.g.*, bicarbonate and carbonate ions) are involved in enamel mineralization. The other implication of this baseline shift is that the mechanisms in which DIC is incorporated into bioapatite are likely influenced by the different growth patterns and mineralization geometries of the two tooth types. Our micro-CT based mineral density results also suggest a slightly higher mineral density (*ca.* +5%) in the mature canine enamel compared to that of the M3. Future studies that specifically target the differences between the tooth types will provide insights into the geochemical processes involved in enamel mineralization and improve our ability to reliably interpret stable isotope results.

4.4. Interpreting canine and M3 $\delta^{18}O$ profiles: implications for environmental reconstruction

Using enamel oxygen isotope variation as an environmental indicator relies on the assumption that the animal's body water follows a predictable pattern that is correlated with environmental conditions. Depending on the physiology, mammalian herbivores can be grouped into evaporation sensitive or evaporation insensitive groups (Blumenthal et al., 2017; Levin et al., 2006). Warthogs (*Phacochoerus* spp.) have been considered evaporation insensitive, the body water of which has been assumed to closely follow isotopic changes in environmental water (Levin et al., 2006; Reid et al., 2019). Although there is a large uncertainty associated with the inverse modeling process, reconstructing timelines of unattenuated seasonal isotopic signal is an essential step towards investigating the relationship between body water isotopes and environmental factors. The intention of the inverse model is to provide a basis for interpreting intra-tooth samples obtained from both canine and molar enamel. The small discrepancy between the model output and measured canine $\delta^{18}O$ profiles (Fig. 8) indicates that suid canines show low levels of seasonal signal damping and may provide close estimates of body water isotopic input. This is likely due to the weak attenuation effect associated with thin enamel in the mineralization process (Zazzo et al., 2012). However, this advantage is not necessarily applicable in paleoecological studies due to the suboptimal preservation and relatively low abundance of suid canines in the fossil record. Additional concerns may evolve around a potentially higher susceptibility to diagenesis in thin enamel (Kohn et al., 1999; Schoeninger et al., 2003; Zazzo et al., 2004, 2012). Nevertheless, intra-tooth sampling in canines is promising in archeological settings in which well-preserved canines of domestic or wild pigs may offer information on environment conditions or seasonal activities, as demonstrated by Frémondeau et al. (2012).

Warthog M3s are found in greater abundances and are better preserved than canines in archeological and paleontological sites, which makes them a potential proxy for paleoenvironmental reconstructions, as reported in Reid et al. (2019). The discrepancy between the interpreted seasonal intervals in modeled unattenuated seasonal timeline and M3 timelines supports previous observations that signal attenuation effect in the enamel maturation process changes the shape of the original input curve, which may affect interpretations of the timing of individual seasons (Green et al., 2018b; Passey and Cerling, 2002; Passey et al., 2005a; Zazzo et al., 2010). On the other hand, when seasonal interpretation is based on a complete seasonal cycle by combining one rainy season and one dry season, the consistency can be as high as 75%. Most of eastern Africa today experiences two rainy seasons per year: one longer season typically from March to May, and a shorter season from October to November (Herrmann and Mohr, 2011; Nicholson, 2017; Yang et al., 2015), which is generally the case in Laikipia (Caylor et al., 2019; Soderberg et al., 2013; Terzer et al., 2013). Although we do not have enough information on how the M3 profiles correlate with rainfall records or precipitation isotope variation in Laikipia, the estimated durations of seasonal cycles are consistent with a bimodal seasonal rainfall pattern with one long rainy season and one short rainy season (Table 5). This suggests that our timeline reconstruction methods can be used to investigate the pattern of rainfall seasonality in archeological and paleontological settings, potentially distinguishing bimodal seasonal rainfall pattern from a unimodal pattern. Combining existing climatic record and local seasonal regimes of the past, for example, can provide better environmental context for prehistoric human activities in Africa such as subsistence strategies, population dynamics, and cultural change (*e.g.*, Henn et al., 2008; Hildebrand and Grillo, 2012; Marshall and Hildebrand, 2002; Skoglund et al., 2017; Tierney and deMenocal, 2013).

Interpreting the amplitudes of $\delta^{18}O$ variation in M3 profiles is more limited at the moment, due to a lack of an appropriate, accessible mathematical model to directly reconstruct the original seasonal input signal. Our estimate of the percentage of seasonal signal preserved in M3 profiles may allow better comparisons of M3 profiles to canine $\delta^{18}O$ profiles. However, it is associated with a large uncertainty that is mainly derived from two sources: 1) the small signal of local $\delta^{18}O$ variation in the profiles; and 2) the large “noise” that is associated with many possible solutions in the inverse model. This limitation will be difficult to improve since the original seasonal input signal is always larger than measured molar enamel isotopic variation. In comparison, using the full range of $\delta^{18}O$ change in the M3 profile produced smaller uncertainty, primarily because this overall signal is by nature larger than any local $\delta^{18}O$ signal identified from only parts of the profiles. Based on the correlation between intra-annual isotope range in precipitation and aridity, the intra-tooth total $\delta^{18}O$ range has been used to reconstruct aridity at various fossil sites in eastern Africa (Blumenthal et al., 2019). Our results provide no evaluation of this method but confirm that making fewer assumptions is potentially associated with a lower uncertainty. Based on the low amplitude of change in $\delta^{18}O$ profiles of warthog M3s, Reid et al. (2019) concluded that the climate during the African Humid Period in Somalia is less seasonal than it is today. Following Blumenthal et al. (2019), however, an alternative interpretation is that the low amplitude could be a result of lower aridity, which is consistent with the context of the African Humid Period, but inconsistent with the water deficit estimates using a separate dataset as reported in Reid et al. (2019). Due to the inconsistent interpretations of aridity based on different datasets, using amplitudes of $\delta^{18}O$ variation in warthog M3 profiles in paleoenvironmental reconstructions may require further scrutiny.

Lastly, seasonal interpretations based on $\delta^{18}O$ profiles depend on how easily recognized the seasonal patterns are. For example, the lack of substantial $\delta^{18}O$ change in the middle of the MPL1 canine and molar profiles makes interpretation of seasonality difficult. This occurred in previous studies in which variation patterns in $\delta^{18}O$ are not easily interpreted (*e.g.*, Lüdecke et al., 2016; Nelson, 2005). We also acknowledge the fact that even the unattenuated seasonal isotopic profiles are not always faithful representations of seasonal environmental changes, as animals are free to move on the landscape and change drinking/food water sources of different isotopic signatures. This factor undoubtedly complicates the situation when interpreting intra-tooth isotope profiles originated in areas of more complex seasonal patterns, such as eastern Africa. Due to these limitations, multiple isotope profiles are necessary to interpret seasonal patterns with relative confidence.

4.5. Case study: revisiting seasonal rainfall during the African Humid Period

The recently published warthog intra-tooth M3 profiles include several *Phacochoerus* sp. intra-tooth profiles from Naivasha, Kenya, and from the Late Pleistocene/Holocene archeological sites Gogoshiis Qabe and Guli Waabayo (2.99° N, 44.30° E) in southern Somalia (Reid et al., 2019). Here we present a case study investigating the pattern of seasonality using our interpretive framework. We selected the specimens that are reported to have complete cervices, so that our enamel extension rate regression can be applied with relative confidence. We reconstructed the molar timeline using the growth rate estimates from a combined M3 extension rate regression (Supplementary S1) and stable isotope intra-tooth sampling distance from the cervix, reported in Reid et al. (2019). Results of the timeline reconstruction are reported in Supplementary S2. We interpreted dry and rainy seasons based on the pattern of $\delta^{18}O$ change in the M3 profiles and calculated the durations of seasonal cycles (Supplementary Fig. S8 and Table S5). We found that three out of four extant warthog profiles show seasonal cycle durations that are consistent with the bimodal rainfall pattern of Naivasha, Kenya. One extant warthog profile shows a seasonal cycle duration that is consistent with a unimodal rainfall pattern. In comparison, both archeological warthogs from Somalia show seasonal cycle durations that are consistent with the bimodal rainfall pattern of the locality today, except for one seasonal cycle that can be assigned to a unimodal rainfall pattern. One potential confounding factor of our interpretation is the assumption that the common warthog (*Phacochoerus africanus*) shares the same enamel growth pattern as the desert warthog (*Phacochoerus aethiopicus*) that is found in Somalia today (d'Huart and Grubb, 2001). Overall, this case study indicates that timeline reconstruction can be used to estimate the duration of dry and rainy seasons using warthog M3s from the paleontological or archeological records. It also suggests that multiple profiles (3–5) should be used to permit seasonal pattern interpretation with relative confidence.

5. Conclusions

This study established growth and mineralization patterns in warthog canine and third molar enamel and explored how they differ and how they can guide the interpretation of intra-tooth isotope profiles. We found near-constant enamel extension rates in the canine and a linear decrease in the growth rate of third molar enamel. For canines, we show that there is an almost immediate onset of enamel mineralization after secretion and a consistent mineralization geometry, whereas in M3s there is a substantial pause after secretion and general increase in the angle of the mineralization front in the third molar enamel. With the canine growth and mineralization data, we used the inverse model to reconstruct unattenuated isotope timeline using canine profiles. Measured canine $\delta^{18}O$ profiles capture 80% of the unattenuated seasonal isotopic signal. In comparison, third molar profiles capture only 50% of the signal per season, and 60% of the total $\delta^{18}O$ range. 75% of the interpreted seasonal cycle durations from the molar timelines are consistent with those of the unattenuated canine timelines. This study evaluated the feasibility of the inverse model for warthog canines and molars. We determined that the model is suitable for canines, and we established the input parameters for the inverse method. Our results suggest that enamel extension rates and maturation geometry are essential in mathematical modeling efforts to reconstruct the unattenuated isotopic signal. Our approach to evaluate and determine the amplitude and duration of seasonality is an important first step in building an interpretive framework around intra-tooth profiles in warthogs. Timeline reconstructions based on M3 $\delta^{18}O$ profiles can be used to investigate the pattern of rainfall seasonality in the past. We found a ~2‰ carbon isotope spacing between canine and third molar enamel, which suggests caution in comparing diets based on stable carbon isotopes from suid canines and molars. This difference may also provide clues into differential formation processes in canine and molar teeth.

Declaration of competing interest

The authors declare that they have no known competing financial interests or personal relationships that could have appeared to influence the work reported in this paper.

Acknowledgements

We would like to thank Dino Martins, Louise Leakey, Meave Leakey, Martin Kirinya, Joséphine Lesur, and the Kenya Wildlife Service for collection, permission, and assistance in accessing the specimens used in this study. We thank John Gitonga, Kelly Caylor, and staff members at Mpala for managing and sharing the meteorological dataset. We thank Ronan Ledevin for assistance with micro-CT scans (UMR CNRS 5199-PACEA microtomography platform). We thank Suvankar Chakraborty for technical support at the SIRFER facility. We thank Daniel Green, Scott Blumenthal, and Gregory Henkes for helpful discussions that improved this manuscript. We thank Robin B. Trayler and one anonymous reviewer for their constructive comments that improved this manuscript. This project is supported by the Leakey Foundation, Sigma Xi Grants in Aid of Research [G2017031588721189], the LaScArBx program [ANR-10-LABX-52], European Commission H2020 Marie Skłodowska-Curie Actions Program [Grant number 798117], the NSF through the ITCE program at the University of Utah, and the Turkana Basin Institute.

Data availability

Additional methods and discussions are available in Supplementary S1 (Appendix A). Raw measurements are available in Supplementary S2 (Appendix A). Additional data (Supplementary S2) are available through Mendeley at https://data.mendeley.com/datasets/3mv45xcp65/1.

Appendix A. Supplementary data

Supplementary data to this article can be found online at https://doi.org/10.1016/j.chemgeo.2020.119799.

References

Ambrose, S.H., DeNiro, M.J., 1986. The isotopic ecology of East African mammals. Oecologia 69 (3), 395–406.
Balasse, M., 2002. Reconstructing dietary and environmental history from enamel isotopic analysis: time resolution of intra-tooth sequential sampling. Int. J. Osteoarchaeol. 12 (3), 155–165.
Balasse, M., Tresset, A., Ambrose, S., 2006. Stable isotope evidence ($\delta^{13}C$, $\delta^{18}O$) for winter feeding on seaweed by Neolithic sheep of Scotland. J. Zool. 270 (1), 170–176.
Behrensmeyer, A.K., 1978. Taphonomic and ecologic information from bone weathering. Paleobiology 4 (2), 150–162.
Bendrey, R., Vella, D., Zazzo, A., Balasse, M., Lepetz, S., 2015. Exponentially decreasing tooth growth rate in horse teeth: implications for isotopic analyses. Archaeometry 57 (6), 1104–1124.
Beniash, E., Metzler, R.A., Lam, R.S.K., Gilbert, P.U.P.A., 2009. Transient amorphous calcium phosphate in forming enamel. J. Struct. Biol. 166 (2), 133–143.
Bernard, A., Daux, V., Lécuyer, C., Brugal, J.-P., Genty, D., Wainer, K., Gardien, V., Fourel, F., Jaubert, J., 2009. Pleistocene seasonal temperature variations recorded in the $\delta^{18}O$ of *Bison priscus* teeth. Earth Planet. Sci. Lett. 283 (1–4), 133–143.
Bishop, L.C., King, T., Hill, A., Wood, B., 2006. Palaeoecology of *Kolpochoerus heseloni* (=*K. limnetes*): a multiproxy approach. Trans. R. Soc. S. Afr. 61 (2), 81–88.
Blumenthal, S.A., Cerling, T.E., Chritz, K.L., Bromage, T.G., Kozdon, R., Valley, J.W., 2014. Stable isotope time-series in mammalian teeth: in situ $\delta^{18}O$ from the innermost enamel layer. Geochim. Cosmochim. Acta 124, 223–236.
Blumenthal, S.A., Levin, N.E., Brown, F.H., Brugal, J.-P., Chritz, K.L., Harris, J.M., Jehle, G.E., Cerling, T.E., 2017. Aridity and hominin environments. Proc. Natl. Acad. Sci. U. S. A. 114 (28), 7331–7336.
Blumenthal, S.A., Cerling, T.E., Smiley, T.M., Badgley, C.E., Plummer, T.W., 2019. Isotopic records of climate seasonality in equid teeth. Geochim. Cosmochim. Acta 260, 329–348.

Bocherens, H., Koch, P.L., Mariotti, A., Geraads, D., Jaeger, J.-J., 1996. Isotopic biogeochemistry (^{13}C, ^{18}O) of mammalian enamel from African Pleistocene hominid sites. Palaios 306–318.
Bowen, G.J., 2008. Spatial analysis of the intra-annual variation of precipitation isotope ratios and its climatological corollaries. J. Geophys. Res. Atmos. 113 (D5).
Bronckers, A.L.J.J., 2017. Ion transport by ameloblasts during amelogenesis. J. Dent. Res. 96 (3), 243–253.
Bryant, D.J., Froelich, P.N., 1995. A model of oxygen isotope fractionation in body water of large mammals. Geochim. Cosmochim. Acta 59 (21), 4523–4537.
Bryant, D.J., Koch, P.L., Froelich, P.N., Showers, W.J., Genna, B.J., 1996. Oxygen isotope partitioning between phosphate and carbonate in mammalian apatite. Geochim. Cosmochim. Acta 60 (24), 5145–5148.
[dataset]Caylor, K., Gitonga, J., Martins, D., 2019. Mpala Research Centre Meteorological and Hydrological Dataset. Mpala Research Centre, Laikipia, Kenya.
Cerling, T.E., Harris, J.M., 1999. Carbon isotope fractionation between diet and bioapatite in ungulate mammals and implications for ecological and paleoecological studies. Oecologia 120 (3), 347–363.
Cerling, T.E., Ayliffe, L.K., Dearing, M.D., Ehleringer, J.R., Passey, B.H., Podlesak, D.W., Torregrossa, A.-M., West, A.G., 2007. Determining biological tissue turnover using stable isotopes: the reaction progress variable. Oecologia 151 (2), 175–189.
Cerling, T.E., Mbua, E., Kirera, F.M., Manthi, F.K., Grine, F.E., Leakey, M.G., Sponheimer, M., Uno, K.T., 2011. Diet of *Paranthropus boisei* in the early Pleistocene of East Africa. Proc. Natl. Acad. Sci. U. S. A. 108 (23), 9337–9341.
Cerling, T.E., Andanje, S.A., Blumenthal, S.A., Brown, F.H., Chritz, K.L., Harris, J.M., Hart, J.A., Kirera, F.M., Kaleme, P., Leakey, L.N., 2015. Dietary changes of large herbivores in the Turkana Basin, Kenya from 4 to 1 Ma. Proc. Natl. Acad. Sci. U. S. A. 112 (37), 11467–11472.
Chenery, C.A., Pashley, V., Lamb, A.L., Sloane, H.J., Evans, J.A., 2012. The oxygen isotope relationship between the phosphate and structural carbonate fractions of human bioapatite. Rapid Commun. Mass Spectrom. 26 (3), 309–319.
Clementz, M.T., 2012. New insight from old bones: stable isotope analysis of fossil mammals. J. Mammal. 93 (2), 368–380.
Cooke, H., Wilkinson, A., 1978. Suidae and Tayassuidae. In: Maglio, V., Cooke, H. (Eds.), Evolution of African Mammals. Harvard University Press, Cambridge, pp. 435–482.
d'Ambrosia, A.R., Clyde, W.C., Fricke, H.C., Chew, A.E., 2014. Stable isotope patterns found in early Eocene equid tooth rows of North America: implications for reproductive behavior and paleoclimate. Palaeogeogr. Palaeoclimatol. Palaeoecol. 414, 310–319.
Damkier, H.H., Josephsen, K., Takano, Y., Zahn, D., Fejerskov, O., Frische, S., 2014. Fluctuations in surface pH of maturing rat incisor enamel are a result of cycles of H^+-secretion by ameloblasts and variations in enamel buffer characteristics. Bone 60, 227–234.
Dansgaard, W., 1964. Stable isotopes in precipitation. Tellus 16 (4), 436–468.
Dean, M.C., 1987. Growth layers and incremental markings in hard tissues; a review of the literature and some preliminary observations about enamel structure in *Paranthropus boisei*. J. Hum. Evol. 16 (2), 157–172.
Dean, M.C., Spiers, K.M., Garrevoet, J., Le Cabec, A., 2019. Synchrotron X-ray fluorescence mapping of Ca, Sr and Zn at the neonatal line in human deciduous teeth reflects changing perinatal physiology. Arch. Oral Biol. 104, 90–102.
d'Huart, J.-P., Grubb, P., 2001. Distribution of the common warthog (*Phacochoerus africanus*) and the desert warthog (*Phacochoerus aethiopicus*) in the Horn of Africa. Afr. J. Ecol. 39 (2), 156–169.
Elliott, J.C., 2002. Calcium phosphate biominerals. Rev. Mineral. Geochem. 48 (1), 427–453.
Farquhar, G.D., Ehleringer, J.R., Hubick, K.T., 1989. Carbon isotope discrimination and photosynthesis. Annu. Rev. Plant Biol. 40 (1), 503–537.
Field, C.R., 1972. The food habits of wild ungulates in Uganda by analyses of stomach contents. Afr. J. Ecol. 10 (1), 17–42.
Frémondeau, D., Cucchi, T., Casabianca, F., Ughetto-Monfrin, J., Horard-Herbin, M.-P., Balasse, M., 2012. Seasonality of birth and diet of pigs from stable isotope analyses of tooth enamel ($\delta^{18}O$, $\delta^{13}C$): a modern reference data set from Corsica, France. J. Archaeol. Sci. 39 (7), 2023–2035.
Fricke, H.C., O'Neil, J.R., 1996. Inter-and intra-tooth variation in the oxygen isotope composition of mammalian tooth enamel phosphate: implications for palaeoclimatological and palaeobiological research. Palaeogeogr. Palaeoclimatol. Palaeoecol. 126 (1), 91–99.
Fricke, H.C., Clyde, W.C., O'Neil, J.R., 1998. Intra-tooth variations in $\delta^{18}O$ (PO_4) of mammalian tooth enamel as a record of seasonal variations in continental climate variables. Geochim. Cosmochim. Acta 62 (11), 1839–1850.
Gat, J.R., 1996. Oxygen and hydrogen isotopes in the hydrologic cycle. Annu. Rev. Earth Planet. Sci. 24 (1), 225–262.
Green, D.R., Green, G.M., Colman, A.S., Bidlack, F.B., Tafforeau, P., Smith, T.M., 2017. Synchrotron imaging and Markov Chain Monte Carlo reveal tooth mineralization patterns. PLoS One 12 (10), e0186391.
Green, D.R., Olack, G., Colman, A.S., 2018a. Determinants of blood water $\delta^{18}O$ variation in a population of experimental sheep: Implications for paleoclimate reconstruction. Chem. Geol. 485, 32–43.
Green, D.R., Smith, T.M., Green, G.M., Bidlack, F.B., Tafforeau, P., Colman, A.S., 2018b. Quantitative reconstruction of seasonality from stable isotopes in teeth. Geochim. Cosmochim. Acta 235, 483–504.
Harris, J.M., Cerling, T.E., 2002. Dietary adaptations of extant and Neogene African suids. J. Zool. 256 (01), 45–54.
Hartman, G., Bar-Yosef, O., Brittingham, A., Grosman, L., Munro, N.D., 2016. Hunted gazelles evidence cooling, but not drying, during the Younger Dryas in the southern Levant. Proc. Natl. Acad. Sci. U. S. A. 113 (15), 3997–4002.
Henn, B.M., Gignoux, C., Lin, A.A., Oefner, P.J., Shen, P., Scozzari, R., Cruciani, F., Tishkoff, S.A., Mountain, J.L., Underhill, P.A., 2008. Y-chromosomal evidence of a pastoralist migration through Tanzania to southern Africa. Proc. Natl. Acad. Sci. U. S. A. 105 (31), 10693–10698.
Herrmann, S.M., Mohr, K.I., 2011. A continental-scale classification of rainfall seasonality regimes in Africa based on gridded precipitation and land surface temperature products. J. Appl. Meteorol. Climatol. 50 (12), 2504–2513.
Higgins, P., MacFadden, B.J., 2009. Seasonal and geographic climate variabilities during the Last Glacial Maximum in North America: applying isotopic analysis and macrophysical climate models. Palaeogeogr. Palaeoclimatol. Palaeoecol. 283 (1–2), 15–27.
Hildebrand, E.A., Grillo, K.M., 2012. Early herders and monumental sites in eastern Africa: dating and interpretation. Antiquity 86 (332), 338–352.
Hoppe, K.A., Stover, S.M., Pascoe, J.R., Amundson, R., 2004. Tooth enamel biomineralization in extant horses: implications for isotopic microsampling. Palaeogeogr. Palaeoclimatol. Palaeoecol. 206 (3), 355–365.
Iacumin, P., Bocherens, H., Mariotti, A., Longinelli, A., 1996. Oxygen isotope analyses of co-existing carbonate and phosphate in biogenic apatite: a way to monitor diagenetic alteration of bone phosphate? Earth Planet. Sci. Lett. 142, 1): 1–6.
Josephsen, K., Takano, Y., Frische, S., Praetorius, J., Nielsen, S., Aoba, T., Fejerskov, O., 2010. Ion transporters in secretory and cyclically modulating ameloblasts: a new hypothesis for cellular control of preeruptive enamel maturation. Am. J. Phys. Cell Physiol. 299 (6), C1299–C1307.
Kierdorf, H., Kierdorf, U., Frölich, K., Witzel, C., 2013. Lines of evidence–incremental markings in molar enamel of Soay sheep as revealed by a fluorochrome labeling and backscattered electron imaging study. PLoS One 8 (9), e74597.
Kierdorf, H., Breuer, F., Witzel, C., Kierdorf, U., 2019. Pig enamel revisited – incremental markings in enamel of wild boars and domestic pigs. J. Struct. Biol. 205 (1), 48–59.
Kingdon, J.D., 1988. East African Mammals: An Atlas of Evolution in Africa, Volume 3, Part B: Large Mammals, 3. University of Chicago Press, Chicago.
Kingston, J.D., 2007. Shifting adaptive landscapes: progress and challenges in reconstructing early hominid environments. Am. J. Phys. Anthropol. 134 (S45), 20–58.
Kirsanow, K., Tuross, N., 2011. Oxygen and hydrogen isotopes in rodent tissues: impact of diet, water and ontogeny. Palaeogeogr. Palaeoclimatol. Palaeoecol. 310 (1), 9–16.
Kohn, M.J., 1996. Predicting animal $\delta^{18}O$: accounting for diet and physiological adaptation. Geochim. Cosmochim. Acta 60 (23), 4811–4829.
Kohn, M.J., Cerling, T.E., 2002. Stable isotope compositions of biological apatite. Rev. Mineral. Geochem. 48 (1), 455–488.
Kohn, M.J., Schoeninger, M.J., Valley, J.W., 1998. Variability in oxygen isotope compositions of herbivore teeth: reflections of seasonality or developmental physiology? Chem. Geol. 152 (1), 97–112.
Kohn, M.J., Schoeninger, M.J., Barker, W.W., 1999. Altered states: effects of diagenesis on fossil tooth chemistry. Geochim. Cosmochim. Acta 63 (18), 2737–2747.
Kovács, M., Danyi, R., Erdélyi, M., Fejérdy, P., Dobó-Nagy, C., 2009. Distortional effect of beam-hardening artefacts on microCT: a simulation study based on an in vitro caries model. Oral Surg. Oral Med. Oral Pathol. Oral Radiol. Endod. 108 (4), 591–599.
Lee-Thorp, J.A., 2008. On isotopes and old bones. Archaeometry 50 (6), 925–950.
Levin, N.E., Cerling, T.E., Passey, B.H., Harris, J.M., Ehleringer, J.R., 2006. A stable isotope aridity index for terrestrial environments. Proc. Natl. Acad. Sci. U. S. A. 103 (30), 11201–11205.
Levin, N.E., Simpson, S.W., Quade, J., Cerling, T.E., Frost, S.R., 2008. Herbivore enamel carbon isotopic composition and the environmental context of *Ardipithecus* at Gona, Ethiopia. Geol. Soc. Am. Spec. 446, 215–234.
Longinelli, A., 1984. Oxygen isotopes in mammal bone phosphate: a new tool for paleohydrological and paleoclimatological research? Geochim. Cosmochim. Acta 48 (2), 385–390.
Lüdecke, T., Mulch, A., Kullmer, O., Sandrock, O., Thiemeyer, H., Fiebig, J., Schrenk, F., 2016. Stable isotope dietary reconstructions of herbivore enamel reveal heterogeneous savanna ecosystems in the Plio-Pleistocene Malawi Rift. Palaeogeogr. Palaeoclimatol. Palaeoecol. 459, 170–181.
Luz, B., Kolodny, Y., Horowitz, M., 1984. Fractionation of oxygen isotopes between mammalian bone-phosphate and environmental drinking water. Geochim. Cosmochim. Acta 48 (8), 1689–1693.
Marshall, F., Hildebrand, E., 2002. Cattle before crops: the beginnings of food production in Africa. J. World Prehist. 16 (2), 99–143.
Mason, D.R., 1984. Dentition and age determination of the warthog *Phacochoerus aethiopicus* in Zululand, South Africa. Koedoe 27 (1), 79–119.
van der Merwe, N.J., 2013. Isotopic ecology of fossil fauna from Olduvai Gorge at ca 1.8 Ma, compared with modern fauna. S. Afr. J. Sci. 109 (11 – 12), 1–14.
Müller, W., Nava, A., Evans, D., Rossi, P.F., Alt, K.W., Bondioli, L., 2019. Enamel mineralization and compositional time-resolution in human teeth evaluated via histologically-defined LA-ICPMS profiles. Geochim. Cosmochim. Acta 255, 105–126. https://doi.org/10.1016/j.gca.2019.03.005.
Nacarino-Meneses, C., Jordana, X., Orlandi-Oliveras, G., Köhler, M., 2017. Reconstructing molar growth from enamel histology in extant and extinct *Equus*. Sci. Rep. 7 (1), 15965.
Nelson, S.V., 2005. Paleoseasonality inferred from equid teeth and intra-tooth isotopic variability. Palaeogeogr. Palaeoclimatol. Palaeoecol. 222 (1–2), 122–144.
Nicholson, S.E., 2017. Climate and climatic variability of rainfall over eastern Africa. Rev. Geophys. 55 (3), 590–635.
Nicholson, S.E., 2018. The ITCZ and the seasonal cycle over equatorial Africa. Bull. Am. Meteorol. Soc. 99 (2), 337–348.
Orlandi-Oliveras, G., Nacarino-Meneses, C., Köhler, M., 2019. Dental histology of late Miocene hipparionins compared with extant *Equus*, and its implications for Equidae life history. Palaeogeogr. Palaeoclimatol. Palaeoecol. 528, 133–146.
Passey, B.H., Cerling, T.E., 2002. Tooth enamel mineralization in ungulates: implications for recovering a primary isotopic time-series. Geochim. Cosmochim. Acta 66 (18), 3225–3234.

Passey, B.H., Cerling, T.E., Schuster, G.T., Robinson, T.F., Roeder, B.L., Krueger, S.K., 2005a. Inverse methods for estimating primary input signals from time-averaged isotope profiles. Geochim. Cosmochim. Acta 69 (16), 4101–4116.
Passey, B.H., Robinson, T.F., Ayliffe, L.K., Cerling, T.E., Sponheimer, M., Dearing, M.D., Roeder, B.L., Ehleringer, J.R., 2005b. Carbon isotope fractionation between diet, breath CO_2, and bioapatite in different mammals. J. Archaeol. Sci. 32 (10), 1459–1470.
Pellegrini, M., Lee-Thorp, J.A., Donahue, R.E., 2011. Exploring the variation of the $\delta^{18}O_p$ and $\delta^{18}O_c$ relationship in enamel increments. Palaeogeogr. Palaeoclimatol. Palaeoecol. 310 (1), 71–83.
Podlesak, D.W., Torregrossa, A.-M., Ehleringer, J.R., Dearing, M.D., Passey, B.H., Cerling, T.E., 2008. Turnover of oxygen and hydrogen isotopes in the body water, CO_2, hair, and enamel of a small mammal. Geochim. Cosmochim. Acta 72 (1), 19–35.
R Core Team, 2019. R: A Language and Environment for Statistical Computing. R Foundation for Statistical Computing, Vienna, Austria.
Reade, H., O'Connell, T.C., Barker, G., Stevens, R.E., 2018. Increased climate seasonality during the late glacial in the Gebel Akhdar, Libya. Quat. Sci. Rev. 192, 225–235.
Reid, R.E.B., Jones, M., Brandt, S., Bunn, H., Marshall, F., 2019. Oxygen isotope analyses of ungulate tooth enamel confirm low seasonality of rainfall contributed to the African Humid Period in Somalia. Palaeogeogr. Palaeoclimatol. Palaeoecol. 534, 109272.
Roberts, P., Stewart, M., Alagaili, A.N., Breeze, P., Candy, I., Drake, N., Groucutt, H.S., Scerri, E.M.L., Lee-Thorp, J., Louys, J., Zalmout, I.S., Al-Mufarreh, Y.S.A., Zech, J., Alsharekh, A.M., al Omari, A., Boivin, N., Petraglia, M., 2018. Fossil herbivore stable isotopes reveal middle Pleistocene hominin palaeoenvironment in 'Green Arabia'. Nat. Ecol. Evol. 2 (12), 1871–1878.
Robinson, C., Briggs, H.D., Atkinson, P.J., Weatherell, J.A., 1979. Matrix and mineral changes in developing enamel. J. Dent. Res. 58 (2_suppl), 871–882.
Rodgers, W.A., 1984. Warthog ecology in south east Tanzania. Mammalia 327.
Romanek, C.S., Grossman, E.L., Morse, J.W., 1992. Carbon isotopic fractionation in synthetic aragonite and calcite: effects of temperature and precipitation rate. Geochim. Cosmochim. Acta 56 (1), 419–430.
Schmitz, J.E., Teepe, J.D., Hu, Y., Smith, C.E., Fajardo, R.J., Chun, Y.-H.P., 2014. Estimating mineral changes in enamel formation by ashing/BSE and microCT. J. Dent. Res. 93 (3), 256–262.
Schoeninger, M.J., Hallin, K., Reeser, H., Valley, J.W., Fournelle, J., 2003. Isotopic alteration of mammalian tooth enamel. Int. J. Osteoarchaeol. 13 (1–2), 11–19.
Simmer, J.P., Fincham, A.G., 1995. Molecular mechanisms of dental enamel formation. Crit. Rev. Oral Biol. Med. 6 (2), 84–108.
Skoglund, P., Thompson, J.C., Prendergast, M.E., Mittnik, A., Sirak, K., Hajdinjak, M., Salie, T., Rohland, N., Mallick, S., Peltzer, A., Heinze, A., Olalde, I., Ferry, M., Harney, E., Michel, M., Stewardson, K., Cerezo-Román, J.I., Chiumia, C., Crowther, A., Gomani-Chindebvu, E., Gidna, A.O., Grillo, K.M., Helenius, I.T., Hellenthal, G., Helm, R., Horton, M., López, S., Mabulla, A.Z.P., Parkington, J., Shipton, C., Thomas, M.G., Tibesasa, R., Welling, M., Hayes, V.M., Kennett, D.J., Ramesar, R., Meyer, M., Pääbo, S., Patterson, N., Morris, A.G., Boivin, N., Pinhasi, R., Krause, J., Reich, D., 2017. Reconstructing prehistoric African population structure. Cell 171 (1), 59–71.e21.
Soderberg, K., Good, S.P., O'Connor, M., Wang, L., Ryan, K., Caylor, K.K., 2013. Using atmospheric trajectories to model the isotopic composition of rainfall in central Kenya. Ecosphere 4 (3), art33.
Souron, A., 2017. Diet and ecology of extant and fossil wild pigs. In: Melletti, M., Meijaard, E. (Eds.), Ecology, Conservation and Management of Wild Pigs and Peccaries. Cambridge University Press, Cambridge, pp. 29–38.
Souron, A., Balasse, M., Boisserie, J.-R., 2012. Intra-tooth isotopic profiles of canines from extant *Hippopotamus amphibius* and late Pliocene hippopotamids (Shungura Formation, Ethiopia): insights into the seasonality of diet and climate. Palaeogeogr. Palaeoclimatol. Palaeoecol. 342, 97–110.
Sponheimer, M., Robinson, T., Ayliffe, L., Passey, B., Roeder, B., Shipley, L., Lopez, E., Cerling, T., Dearing, D., Ehleringer, J., 2003. An experimental study of carbon-isotope fractionation between diet, hair, and feces of mammalian herbivores. Can. J. Zool. 81 (5), 871–876.
Suga, S., 1982. Progressive mineralization pattern of developing enamel during the maturation stage. J. Dent. Res. 61, 1532–1542.
Sydney-Zax, M., Mayer, I., Deutsch, D., 1991. Carbonate content in developing human and bovine enamel. J. Dent. Res. 70 (5), 913–916.
Tejada-Lara, J.V., MacFadden, B.J., Bermudez, L., Rojas, G., Salas-Gismondi, R., Flynn, J.J., 2018. Body mass predicts isotope enrichment in herbivorous mammals. Proc. R. Soc. B 285 (1881).
Teklehaimanot, G., Balakrishnan, M., 2017. Population status, feeding ecology and habitat association of the common warthog (*Phacochoerus africanus*) in Bale Mountains National Park, Ethiopia. Int. J. Ecol. Environ. Sci. 43 (3), 185–194.
Terzer, S., Wassenaar, L.I., Araguás-Araguás, L.J., Aggarwal, P.K., 2013. Global isoscapes for $\delta^{18}O$ and $\delta^{2}H$ in precipitation: improved prediction using regionalized climatic regression models. Hydrol. Earth Syst. Sci. 17 (11), 4713–4728.
Tierney, J.E., deMenocal, P.B., 2013. Abrupt shifts in horn of Africa hydroclimate since the Last Glacial Maximum. Science 342 (6160), 843–846.
Tieszen, L.L., Senyimba, M.M., Imbamba, S.K., Troughton, J.H., 1979. The distribution of C_3 and C_4 grasses and carbon isotope discrimination along an altitudinal and moisture gradient in Kenya. Oecologia 37 (3), 337–350.
Trayler, R.B., Kohn, M.J., 2017. Tooth enamel maturation reequilibrates oxygen isotope compositions and supports simple sampling methods. Geochim. Cosmochim. Acta 198, 32–47.
Uno, K.T., Fisher, D., Wittemyer, G., Douglas-Hamilton, I., Carpenter, N., Omondi, P., Cerling, T.E., in press. Forward and inverse methods for extracting climate and diet information from stable isotope profiles in proboscidean molars. Quat. Int. https://doi.org/10.1016/j.quaint.2020.06.030.
Uno, K.T., Quade, J., Fisher, D.C., Wittemyer, G., Douglas-Hamilton, I., Andanje, S., Omondi, P., Litoroh, M., Cerling, T.E., 2013. Bomb-curve radiocarbon measurement of recent biologic tissues and applications to wildlife forensics and stable isotope (paleo)ecology. Proc. Natl. Acad. Sci. U. S. A. 110 (29), 11736–11741.
Volchansky, A., Cleaton-Jones, P., Wright, P.G., Fatti, L.P., 1985. Gingival and labial vestibular temperature in young individuals. J. Dent. 13 (4), 323–330.
Yang, W., Seager, R., Cane, M.A., Lyon, B., 2015. The annual cycle of East African precipitation. J. Clim. 28 (6), 2385–2404.
Zazzo, A., Mariotti, A., Lécuyer, C., Heintz, E., 2002. Intra-tooth isotope variations in late Miocene bovid enamel from Afghanistan: paleobiological, taphonomic, and climatic implications. Palaeogeogr. Palaeoclimatol. Palaeoecol. 186 (1–2), 145–161.
Zazzo, A., Lécuyer, C., Mariotti, A., 2004. Experimentally-controlled carbon and oxygen isotope exchange between bioapatites and water under inorganic and microbially-mediated conditions. Geochim. Cosmochim. Acta 68 (1), 1–12.
Zazzo, A., Balasse, M., Patterson, W.P., 2005. High-resolution $\delta^{13}C$ intratooth profiles in bovine enamel: Implications for mineralization pattern and isotopic attenuation. Geochim. Cosmochim. Acta 69 (14), 3631–3642.
Zazzo, A., Balasse, M., Passey, B., Moloney, A., Monahan, F., Schmidt, O., 2010. The isotope record of short-and long-term dietary changes in sheep tooth enamel: implications for quantitative reconstruction of paleodiets. Geochim. Cosmochim. Acta 74 (12), 3571–3586.
Zazzo, A., Bendrey, R., Vella, D., Moloney, A.P., Monahan, F.J., Schmidt, O., 2012. A refined sampling strategy for intra-tooth stable isotope analysis of mammalian enamel. Geochim. Cosmochim. Acta 84, 1–13.
Zou, W., Hunter, N., Swain, M.V., 2011. Application of polychromatic μCT for mineral density determination. J. Dent. Res. 90 (1), 18–30.